SENSORDEVICES 2025

The Sixteenth International Conference on Sensor Device Technologies and Applications

October 26th - 30th, 2025

Barcelona, Spain

SENSORDEVICES 2025 Editors

Narito Kurata, Tsukuba University of Technology, Japan

SENSORDEVICES 2025

Forward

The Sixteenth International Conference on Sensor Device Technologies and Applications (SENSORDEVICES 2025), held between October 26th, 2025, and October 30th, 2025, in Barcelona, Spain, continued a series of events focusing on sensor devices themselves, the technology-capturing style of sensors, special technologies, signal control and interfaces, and particular sensors-oriented applications. The evolution of nano- and micro-technologies, nanomaterials, and the new business services make the sensor device industry and research on the sensors themselves very challenging.

Most sensor-oriented research and industry initiatives are focusing on sensor networks, data security, exchange protocols, energy optimization, and features related to intermittent connections. Recently, the concept of Internet-of-things gathers attention, especially when integrating IPv4 and IIPv6 networks. We welcomed technical papers presenting research and practical results, position papers addressing the pros and cons of specific proposals, such as those being discussed in the standard fora or in industry consortia, survey papers addressing the key problems and solutions on any of the above topics short papers on work in progress, and panel proposals.

We take the opportunity to warmly thank all the members of the SENSORDEVICES 2025 technical program committee, as well as all the reviewers. The creation of such a high-quality conference program would not have been possible without their involvement. We also kindly thank all the authors who dedicated much of their time and effort to contribute to SENSORDEVICES 2025. We truly believe that, thanks to all these efforts, the final conference program consisted of top-quality contributions. We also thank the members of the SENSORDEVICES 2025 organizing committee for their help in handling the logistics of this event.

We hope that SENSORDEVICES 2025 was a successful international forum for the exchange of ideas and results between academia and industry for the promotion of progress in the field of sensor device technologies and applications.

SENSORDEVICES 2025 Chairs

SENSORDEVICES 2025 Steering Committee
Arcady Zhukov, University of Basque Country (UPV/EHU), San Sebastian / Ikerbasque, Basque, Foundation for Science, Bilbao, Spain
Sazzadur Chowdhury, University of Windsor, Canada
Narito Kurata, Tsukuba University of Technology, Japan
Manuela Vieira, CTS/ISEL/IPL, Portugal
Toshihiko Kiwa, Okayama University, Japan

SENSORDEVICES 2025 Publicity Chairs
Lorena Parra Boronat, Universidad Politécnica de Madrid, Spain
Laura Garcia, Universidad Politécnica de Cartagena, Spain

SENSORDEVICES 2025
Committee

SENSORDEVICES 2025 Steering Committee

Arcady Zhukov, University of Basque Country (UPV/EHU), San Sebastian / Ikerbasque, Basque, Foundation for Science, Bilbao, Spain
Sazzadur Chowdhury, University of Windsor, Canada
Narito Kurata, Tsukuba University of Technology, Japan
Manuela Vieira, CTS/ISEL/IPL, Portugal
Toshihiko Kiwa, Okayama University, Japan

SENSORDEVICES 2025 Publicity Chairs

Lorena Parra Boronat, Universidad Politécnica de Madrid, Spain
Laura Garcia, Universidad Politécnica de Cartagena, Spain

SENSORDEVICES 2025 Technical Program Committee

Ahmed Alfadhel, Rochester Institute of Technology, USA / Research Products Development Company, Saudi Arabia
Jesús B. Alonso Hernández, Institute for Technological Development and Innovation in Communications (IDeTIC) | University of Las Palmas de Gran Canaria (ULPGC), Spain
Sebastian Anand Alphonse, LivaNova PLC, Houston, USA
Ahmed Ammar, Ohio Northern University, USA
Darius Andriukaitis, Kaunas University of Technology (KTU), Lithuania
Francisco Arcega, University of Zaragoza, Spain
Aktham Asfour, University Grenoble Alpes | CNRS | Grenoble INP, France
Herve Aubert, Laboratory for Analysis and Architecture of Systems (LAAS-CNRS), Toulouse, France
Ripendra Awal, Prairie View A&M University, USA
Yang Bai, University of Maryland College Park, USA
Orlando R. Baiocchi, University of Washinton Tacoma, USA
Valerio Baiocchi, "Sapienza" University of Rome, Italy
Camelia Bala, University of Bucharest, Romania
Krishnan Balasubramaniam, Indian Institute of Technology Madras, India
Jose Barata, NOVA University of Lisbon, Portugal
Yoseph Bar-Cohen, Jet Propulsion Laboratory | NASA, USA
Michal Borecki, Warsaw University of Technology | Institute of Microelectronics and Optoelectronics, Poland
Christos Bouras, University of Patras, Greece
Manuel José Cabral dos Santos Reis, IEETA / University of Trás-os-Montes e Alto Douro, Portugal
Luigi Campanella, Sapienza University of Rome, Italy
Juan-Carlos Cano, Universitat Politecnica de Valencia, Spain
Nicola Carbonaro, Research Centre "E. Piaggio" | University of Pisa, Italy
Vítor Carvalho**,** 2Ai Lab- School of Technology - IPCA / Algoritmi Research Center - Minho University, Portugal

Paula María Castro Castro, University of A Coruña, Spain
Fulvio Re Cecconi, Politecnico di Milano, Italy
Tao Chen, University of Pittsburgh, USA
Irinela Chilibon, National Institute of Research and Development for Optoelectronics - INOE-2000, Romania
Raad Farhood Chisab, Middle Technical University, Baghdad, Iraq
Nan-Fu Chiu, National Taiwan Normal University, Taiwan
Chi-Wai Chow, National Chiao Tung University, Hsinchu, Taiwan
Sazzadur Chowdhury, University of Windsor, Canada
Jesse R. Codling, University of Michigan - Ann Arbor, USA
Juan M. Corchado, University of Salamanca, Spain
Marco Crescentini, University of Bologna, Italy
Udhaya Kumar Dayalan, Trane Technologies, USA
Francesco G. Della Corte, Università degli Studi di Napoli Federico II, Italy
Emiliano Descrovi, Norwegian University of Science and Technology (NTNU), Trondheim, Norway / Polytechnic University of Turin, Torino, Italy
Abdou Karim Diallo,Gaston Berger University, Senegal
Dermot Diamond, Dublin City University, Ireland
Amad Ud Din, Fatima Jinnah Women University, Pakistan
Toan Dinh, University of Southern Queensland, Australia
Bahram Djafari Rouhani, University of Lille, France
René Domínguez-Cruz, Universidad Autónoma de Tamaulipas, Mexico
Mingzheng Duan, University of California Berkeley, USA
Jimmy T. Efird, CSPEC/DVAHCS/HSR&D (Duke University Affiliated Center), Durham, USA
Abdelali Elmoufidi, Hassan II University of Casablanca, Morocco
Eugenia Fagadar-Cosma, Institute of Chemistry "Coriolan Dragulescu", Timisoara, Romania
Francisco Falcone, UPNA-ISC, Spain
Vittorio Ferrari, University of Brescia, Italy
Laurent Fesquet, Grenoble Institute of Technology, France
Rui Fonseca-Pinto, Polytechnic of Leiria, Portugal
Nazila Fough, Robert Gordon University, UK
Óscar Fresnedo Arias, University of A Coruña, Spain
Mounir Gaidi, University of Sharjah, UAE
Cécile Ghouila-Houri, Centrale Lille, France
Francesca Giannone, Niccolò Cusano University, Rome, Italy
Michele Giordano, IPCB - CNR, Italy
Jan Havlík, Czech Technical University in Prague, Czech Republic
Lukas Heindler, Johannes Kepler University Linz, Austria
Johan Holmgren, Malmö University, Sweden
M. Carmen Horrillo Güemes, Group of Technology of Advanced Sensors (SENSAVAN)-ITEFI-CSIC, Spain
Wen-Jyi Hwang, National Taiwan Normal University, Taipei, Taiwan
Mohamed Ichchou, Ecole Centrale de Lyon, France
Raul Igual, EUP Teruel | University of Zaragoza, Spain
Illyas Md Isa, Universiti Pendidikan Sultan Idris, Malaysia
Kh Tohidul Islam, The University of Melbourne | Melbourne Medical School, Australia
Chi-Shih Jao, University of California, Irvine, USA
Mark Kagarura, Paderborn University, Germany / Makerere University, Uganda
Grigoris Kaltsas, University of West Attica, Greece

Mohamed Kara-Mohamed, Liverpool John Moores University, UK
Rajesh Khanna, Thapar Institute of Engineering and Technology, India
Ahmed Khorshid, Advanced Micro Devices (AMD), USA
Hyunook Kim, University of Seoul, Korea
Farzana Kulsoom, University of Engineering and Technology, Taxila, Pakistan
Narito Kurata, Tsukuba University of Technology, Japan
José Luis Lázaro-Galilea, University of Alcalá, Spain
Ching-Ting Lee, Yuan Ze University / National Cheng-Kung University, Taiwan
Gyu Myoung Lee, Liverpool John Moores University, UK
Kevin Lee, School of InformationTechnology | Deakin University, Melbourne, Australia
Martin Lenzhofer, SiliconAustriaLabsGmbH, Austria
Diego Liberati, National Research Council of Italy, Italy
Kai Lin, eBay Inc., USA
Tong Liu, University of Illinois at Urbana-Champaign, USA
Eduard Llobet, Universitat Rovira i Virgili, Spain
Adrian Luca, Lausanne University Hospital, Switzerland
Jerzy P. Lukaszewicz, Nicoulaus Copernicus University, Torun, Poland
Zhipeng Ma, School of Aeronautics and Astronautics | Zhejiang University, China
Joaquim Miguel Maia, Federal University of Technology - Paraná (UTFPR), Brazil
Oleksandr Makeyev, School of STEM | Diné College, USA
Jorge Marcos Acevedo, University of Vigo, Spain
Stefano Mariani, Politecnico di Milano, Italy
Carlo Massaroni, Università Campus Bio-Medico di Roma, Italy
Vojko Matko, University of Maribor, Slovenia
Demétrio Matos, Polytechnic Institute of Cávado and Ave |School of Design-ID+,Portugal
Carlos Montez, Federal University of Santa Catarina, Brazil
Rafael Morales Herrera, University of Castilla-La Mancha, Spain
Kebria Naderi, Guilan University, Rasht, Iran
Masanari Nakamura, Hokkaido University, Japan
Phendukani Ncube, Gwanda State University, Zimbabwe
Tanzila Noushin, The University of Texas at Dallas, USA
Michal Nowicki, Warsaw University of Technology, Poland
Mehmet Akif Ozdemir, Izmir Katip Celebi University, Turkey
Vinayak Pachkawade, SenseAll, India
Sujata Pal, Indian Institute of Technology, Ropar, India
Lorenzo Palazzetti, University of Perugia, Italy
Evangelos Papadopoulos, National Technical University of Athens, Greece
François Pérès, University of Toulouse, France
Babu Pillai, Southern Cross University, Australia
Ivan Miguel Pires, Instituto de Telecomunicações - Universidade da Beira Interior / Polytechnic Institute
of Viseu, Portugal
R. N. Ponnalagu, BITS Pilani, Hyderabad campus, India
Patrick Pons, CNRS-LAAS, Toulouse, France
Kushal K. Ponugoti, North Dakota State University, USA
Cleonilson Protasio de Souza, Federal University of Paraiba, Brazil
Radislav A. Potyrailo, GE Research, USA
Vaishak Prathap, State University of New York at Buffalo, USA
Antonio L. L. Ramos, University of South-Eastern Norway (USN), Norway

Xiaohong Zhou, Tsinghua University, China
Arkady Zhukov, UPV/EHU, Spain
Daniele Zonta, University of Trento, Italy / University of Strathclyde, UK
Huadi Zhu, Georgia State University, USA

Copyright Information

For your reference, this is the text governing the copyright release for material published by IARIA.

The copyright release is a transfer of publication rights, which allows IARIA and its partners to drive the dissemination of the published material. This allows IARIA to give articles increased visibility via distribution, inclusion in libraries, and arrangements for submission to indexes.

I, the undersigned, declare that the article is original, and that I represent the authors of this article in the copyright release matters. If this work has been done as work-for-hire, I have obtained all necessary clearances to execute a copyright release. I hereby irrevocably transfer exclusive copyright for this material to IARIA. I give IARIA permission or reproduce the work in any media format such as, but not limited to, print, digital, or electronic. I give IARIA permission to distribute the materials without restriction to any institutions or individuals. I give IARIA permission to submit the work for inclusion in article repositories as IARIA sees fit.

I, the undersigned, declare that to the best of my knowledge, the article is does not contain libelous or otherwise unlawful contents or invading the right of privacy or infringing on a proprietary right.

Following the copyright release, any circulated version of the article must bear the copyright notice and any header and footer information that IARIA applies to the published article.

IARIA grants royalty-free permission to the authors to disseminate the work, under the above provisions, for any academic, commercial, or industrial use. IARIA grants royalty-free permission to any individuals or institutions to make the article available electronically, online, or in print.

IARIA acknowledges that rights to any algorithm, process, procedure, apparatus, or articles of manufacture remain with the authors and their employers.

I, the undersigned, understand that IARIA will not be liable, in contract, tort (including, without limitation, negligence), pre-contract or other representations (other than fraudulent misrepresentations) or otherwise in connection with the publication of my work.

Exception to the above is made for work-for-hire performed while employed by the government. In that case, copyright to the material remains with the said government. The rightful owners (authors and government entity) grant unlimited and unrestricted permission to IARIA, IARIA's contractors, and IARIA's partners to further distribute the work.

Table of Contents

Predictive Inspection of Vegetation Encroachment on Power Lines using Line-Crawling Robot and Multimodal Sensor

Alexandre Domingues, Oswaldo Ramos Neto, José Mário Nishihara, Davi Riiti Goto do Valle,
Ronnier Frates Rohrich ⓘD and Andre Schneider de Oliveira ⓘD
Graduate Program in Electrical and Computer Engineering
Graduate Program in Computer Science
Universidade Tecnológica Federal do Paraná
Curitiba, Brazil
e-mail:{alexandredomingues|oswaldo|josalb|daviriiti}@alunos.utfpr.edu.br
{rohrich|andreoliveira}@utfpr.edu.br

Abstract—This paper presents an approach for the predictive inspection of high-voltage transmission lines utilizing a multimodal sensor mounted on an autonomous robot capable of navigating the transmission cables and overcoming obstacles. The primary aim is to assess the proximity of vegetation to the power lines and to predict potential electrical faults, such as arcing and current leaks, which could lead to outages or safety hazards. This intelligent, sensor-driven method enhances early fault detection, contributing to improved maintenance strategies and increased reliability of the power transmission infrastructure.

Keywords-robot; inspection; predictive; vegetation.

I. Introduction

Inspection of high-voltage power lines is critical in ensuring reliable and safe electricity transmission between the generation and great centers. Systematic inspections are vital to identify potential faults, assess infrastructure integrity, and implement repairs to mitigate disruptions and enhance the longevity of the power grid system [1].

Corrective maintenance is very costly because it occurs after a failure, and the time required for maintenance is directly related to the time without a power supply to large centers. Preventive maintenance is used as a periodic tool to guarantee the longevity of transmission lines, but it leads to frequent unnecessary equipment replacement, resulting in unnecessary costs [2]. The ideal solution is to use predictive maintenance, which occurs through a correct inspection diagnosis and leads to changes or corrections that are truly necessary for the continuity of electrical energy transmission.

Predictive inspection of high-voltage power lines without the assistance of robotic technology presents considerable challenges due to the inaccessible and hazardous environments in which these lines are situated and because it is necessary for a rigorous diagnostic. Human inspection requires significant resource allocation, including deploying helicopters or other specialized equipment, which can be costly and time-consuming. These inspections are prone to human error and may not consistently identify all defects [3].

Vegetation encroachment is a critical issue for power transmission lines because of the growth of trees and other vegetation into the clearance zones around high-voltage lines, which can pose significant risks to the reliability and safety of power distribution networks. When vegetation contacts power lines or equipment, it can lead to interruptions and electrical faults, including short circuits and grounding faults that may result in power outages. An electric arc must be created with an arc fuge, which can lead to burning vegetation and nearby areas [4].

The remainder of this paper is structured as follows. Section 2 presents the proposed multimodal inspection approach, detailing the sensing technologies and data acquisition strategies adopted for high-voltage transmission line monitoring. Section 3 focuses on predictive inspection of vegetation encroachment, describing the analytical methods and algorithms applied to assess proximity risks and enable early fault detection. Finally, Section 4 concludes the paper by summarizing the main contributions and outlining directions for future work.

II. Multimodal inspection

Multimodal inspection of power lines involves integrating various sensing and data acquisition techniques to comprehensively monitor the transmission infrastructure's health and safety [5]. The MultiSpectrum sensor aims to enable the detection of a wide range of issues, such as damages, vegetation encroachment, thermal anomalies, and corrosion, combining technologies such as visual imaging, infrared thermography, multispectral sensors, and depth sensors, as shown in Figure 1. The synergy of multiple inspection modalities provided by this sensor produces a more detailed and more accurate assessment than any single method could achieve alone, allowing early fault detection.

The *Power Transmission Lines Inspection Robot* (PTLIR) is line-crawling robot that moves on transmission line cables, overcoming obstacles, such as spacers, insulators, and conductor path variations. The topology aims to ensure efficient cable adhesion and perform evasive maneuvers without external intervention. The robot disengages its wheels from the cable, surpasses the obstacle, and reestablishes contact and traction to continue moving, offering a practical approach for future autonomous inspection systems. As Figure 2 illustrates, this robot moves the MultiSpectrum robot above the power lines.

From a technical point of view, the robot has six degrees of freedom distributed among its main mechanisms: two degrees

01 – spectral camera
02 – embedded electronics
03 – thermal and RGB camera
04 – acoustic camera
05 – cable holder
06 – RGB and depth camera
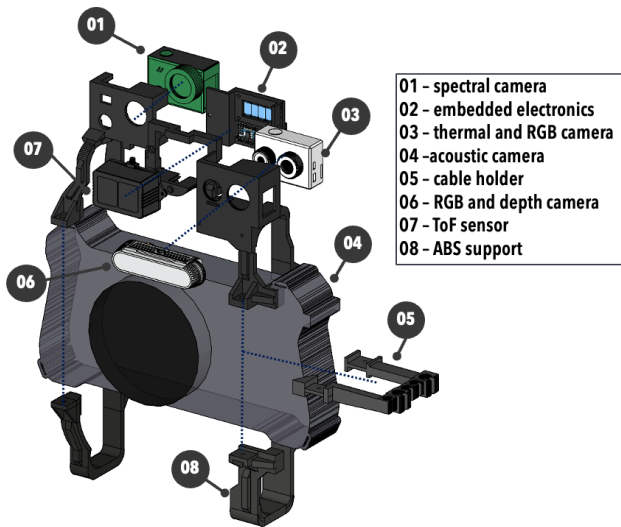07 – ToF sensor
08 – ABS support
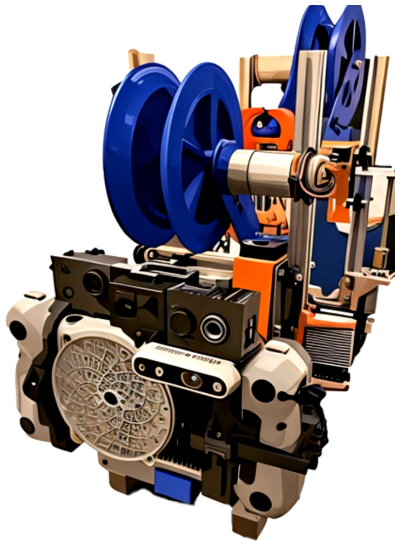
Figure 1. Multimodal inspection sensor [3].

Figure 2. RPTLIR robot with MultiSpectrum inspection sensor.

for the traction wheels, which separate laterally to release the cable; two degrees in the lifting mechanisms, which move the wheels vertically to bypass obstacles; one degree of freedom in the wheelbase opening and closing system, adjusting the robot's width as needed; and an additional degree corresponding to the closure of the claw that secures the robot to the cable during operations. This combination of movements enables the system to perform complex bypass maneuvers with precision while maintaining its mechanical fixation and alignment along the line.

The MultiSpectrum sensor generates a composite inspection map in which each layer represents a specific integrity analysis. The map is spatially and temporally referenced, allowing the status of electrical power elements to be determined at specific times. Predicting future behavior and potential failure progression is possible by correlating different inspection maps

for the same elements, as shown in Figure 3.
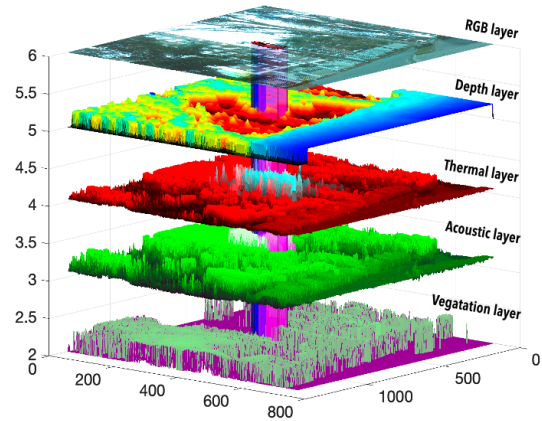
Figure 3. Multilayer Inspection Map.

III. PREDICTIVE INSPECTION OF VEGETATION ENCROACHMENT

Invasive vegetation inspection is carried out using a multispectral camera that is a module of a MultiSpectrum sensor and captures detailed spectral data across multiple wavelengths, assessing vegetation health. By analyzing specific spectral bands — particularly those associated with chlorophyll absorption and reflectance, such as the red, green, and near-infrared regions — the camera can detect subtle variations in plant vitality that are not visible to the naked eye. This capability enables precise assessment of plant health, stress levels, and potential issues such as disease or inadequate water supply. This information is directly related to the distance of vegetation from the power lines and the current fugue that causes the electric arc, as illustrated in Figure 4.
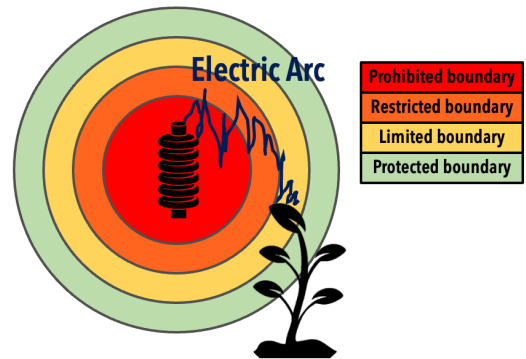
Figure 4. Electric arc occurrence on Vegetation Encroachment.

The multispectral image is segmented using k-means clustering in the Lab color space. The process begins by loading the image and converting it from sRGB to improved perceptual uniformity. The 'a*' and 'b*' channels, which carry color information, are then extracted. The pixel data is reshaped into a two-dimensional matrix and clustered into three groups using k-means, with multiple iterations to enhance the clustering accuracy. The resulting cluster labels are reshaped back into

the original image dimensions, producing a labeled image and separate segmented images for each cluster, where only the pixels belonging to a specific cluster are visible. This method effectively groups the image based on color similarities, enabling a detailed analysis of different regions. The segmented results are subsequently mapped onto the RPB classified layer of the inspection map to identify the regions of the transmission line elements and to generate three-dimensional security boundaries for a comprehensive assessment of the infrastructure, as shown in Figure 5.

Figure 5. Multispectral imagem processing.

IV. CONCLUSION AND FUTURE WORK

This paper discussed the use of multimodal sensors on autonomous robots for predictive inspection of high-voltage transmission lines, enabling accurate assessment of vegetation proximity and early detection of electrical faults. Future work should focus on refining sensor integration for real-time data processing, expanding autonomous navigation capabilities in diverse environmental conditions, and developing advanced algorithms for predictive analytics to improve fault prediction accuracy and inspection automation further.

Additional experiments with more detailed data processing results are currently being developed. These include the presentation of larger datasets, numerical matrices, and complete examples of image and sensor data processing workflows. As the research progresses, these results will provide a more comprehensive view of the methodology and its performance under different operational conditions, contributing to the robustness and scalability of the proposed approach.

ACKNOWLEDGMENTS

REFERENCES

[1] W. Zheng, T. Hui, L. Bing, X. Bingyang, and L. Junnan, "Research on image recognition and processing algorithm of power grid inspection based on uav", in *2024 IEEE 4th International Conference on Electronic Technology, Communication and Information (ICETCI)*, 2024, pp. 1213–1220.

[2] A. Pagnano, M. Höpf, and R. Teti, "A roadmap for automated power line inspection. maintenance and repair", *Procedia Cirp*, vol. 12, pp. 234–239, 2013.

[3] J. M. N. De Albuquerque et al., "A novel method for multi-modal predictive inspection of power lines", *IEEE Access*, 2024.

[4] F. Mahdi Elsiddig Haroun, S. N. Mohamed Deros, M. Z. Bin Baharuddin, and N. Md Din, "Detection of vegetation encroachment in power transmission line corridor from satellite imagery using support vector machine: A features analysis approach", *Energies*, vol. 14, no. 12, 2021.

[5] Q. Liu, "Building an adaptive inspection robot system to improve the quality of power transmission line operation and maintenance in mountainous areas", in *2025 2nd International Conference on Intelligent Computing and Robotics (ICICR)*, 2025, pp. 569–574.

Development of a Customized Multi-sensory Detection Tactile Sensor Module for Commercial Robot Hands

Jin-Seok Jang
Convergence Research Center for Meta-Touch
Korea Research Institute of Standards and Science
Daejeon, Republic of Korea
e-mail: jang82@kriss.re.kr

Bo-Gyu Bok
Convergence Research Center for Meta-Touch
Korea Research Institute of Standards and Science
Daejeon, Republic of Korea
e-mail: wcsp@kriss.re.kr

Min-Seok Kim
Convergence Research Center for Meta-Touch
Korea Research Institute of Standards and Science
Daejeon, Republic of Korea
e-mail: minsk@kriss.re.kr

Abstract— **We have developed a hybrid tactile sensor module that is customized for the Allegro robot hand, a commercial robot hand. The tactile sensor module consists of a 3-axis force sensor and temperature sensor and pressure sensor. Four commercial semiconductor strain gauges are attached to a specially designed metal mechanism to implement the three-axis force sensor. Based on the three-axis force measurements, it detects various physical quantities such as the direction, magnitude, and vibration of the force. The pressure sensor consists of a total of 64 high-performance pressure cells arranged in an 8 x 8 array, covering an area of about 3 cm x 3 cm to detect pressure distribution with high spatial resolution. The temperature sensor uses a commercial thermistor capable of measuring from -10°C to 80°C to detect the object's temperature. We have demonstrated through experiments that the robot fingertip module developed can detect various senses using the internal 3-axis force sensor, pressure sensor, and temperature sensor.**

Keywords-tactile sensor module; 3 axis force; pressure; temperature; robot hand.

I. INTRODUCTION

The advancement of robotics has enabled robots to play a significant role in daily life and industrial environments. However, robots still show a substantial difference in their ability to manipulate objects compared to humans. The superior manipulation ability of the human hand arises from its ability to integrate various sensory information to handle objects precisely. Significant progress is needed to implement such abilities in robotic hands, with tactile sensing being the most crucial aspect. Tactile sensing is the ability to detect various physical quantities, such as pressure, vibration, and temperature. Human tactile sensing capability is determined by the mechanoreceptors distributed at the fingertips [1][2]. These receptors are located in the dermis and epidermis of the skin. To implement sensors that mimic the structure of human skin, a hybrid structure is required.

In this study, we developed a robot fingertip-shaped hybrid tactile sensor module integrating three-axis force, pressure, and temperature sensors to meet these requirements. Experiments were conducted to confirm the sensing characteristics of each sensor.
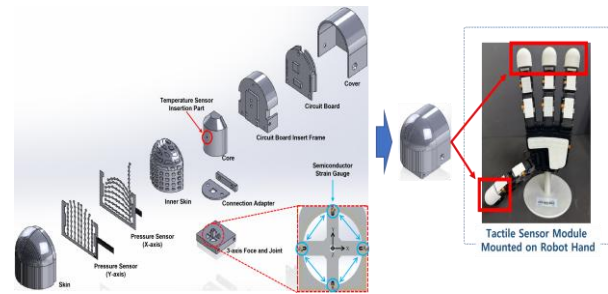
Figure 1. Configuration and Assembly View of Tactile Sensor Module.

Our development will be explained by dividing it into the following sections. Section 2 explains the design and production method of the developed product, Section 3 discusses the characteristics of each sensor in the paper, and the final conclusion includes the results and future plans of the work.

II. DESIGN AND FABRICATION

A. Design

In order to realize multi-sensory detection at the fingertips of the robot, a tactile sensor module was designed using an aluminum metal frame and a silicone rubber mold. The Maltese cross-type metal frame houses a three-axis force sensor and a temperature sensor at the core of the module. The silicone rubber mold can accommodate an 8 x 8 pressure sensor array. The overall size of the tactile sensor module is designed to be about 30 mm x 30 mm x 25 mm, allowing for the integration of three sensors and driving boards within this area. Figure 1 shows the complete configuration and assembly of the module. The ultimate goal of our research and development is to customize the tactile sensor module for various robot hands and apply it practically.

B. Fabrication

The three-axis force sensor, consisting of a Maltese cross-type metal frame, takes advantage of the physical characteristics of this structure. Four commercial 'U'-shaped semiconductor strain gauges (USA) are placed at optimal positions on this frame to improve the ability to detect various forces. Additionally, the central pillar part of the structure has been expanded to increase the sensor's sensitivity. Commercial thermistors (SHIBAURA Electronics Co., LTD., JAPAN) are placed in a hole in the center of the core to detect the temperature of an object in contact with the sensor. The epidermis is designed to detect the pressure of the entire fingertip using a silicone rubber mold that mimics the form of human fingertips and integrates 64 high-performance pressure cells. A Flexible Printed Circuit Board (FPCB) is required to attach a flat FPCB sensor to the three-dimensional surface of the fingertip.

Figure 2. Components of Module.   Figure 3. Assembled Module.

This is achieved by dividing the pressure sensor into the X-axis and Y-axis layers. The pressure cells are manufactured by screen printing pressure-sensing ink onto an electrode made of FPCB. The three-axis force, pressure, and temperature sensors had to be miniaturized to integrate the driving board that measures the signal into the module. This is achieved by designing the PCB as a multilayer structure and compactly integrating all the required components into the robot fingertip module. Figures 2 and 3 show the components and assembled module of the tactile sensor module with robot fingertips.

III.   EVALUATION

The performance of the tri-axial force, pressure, and temperature sensors embedded in the robotic fingertip-shaped tactile sensor module was evaluated.

The pressure sensor of module was evaluated using a precision scale and a tri-axial translation stage. The pressure detection range was 3 to 20 N (Figure 4 (a), (b)).

For the tri-axial force sensor, the evaluation was conducted according to the ISO 376 international standard [DIN EN ISO 376:2011] calibration procedure using a 20 N deadweight force standard device at the Korea Research Institute of Standards and Science. The sensor's detection characteristics were observed by applying loads in the vertical and horizontal directions. When vertical forces Fz up to 10 N and horizontal forces Fx and Fy up to 5 N were

applied (see Figure 5 (a), (b), (c)), the sensor demonstrated a repeatability error of less than 0.5%, hysteresis error of less than 0.5%, and non-linearity error of less than 1.5 % (Figure 5 (c)). Crosstalk between the X and Y axes during horizontal force measurements was within approximately 3%, indicating minimal interference between the axes (Figure 5 (a), (b)).
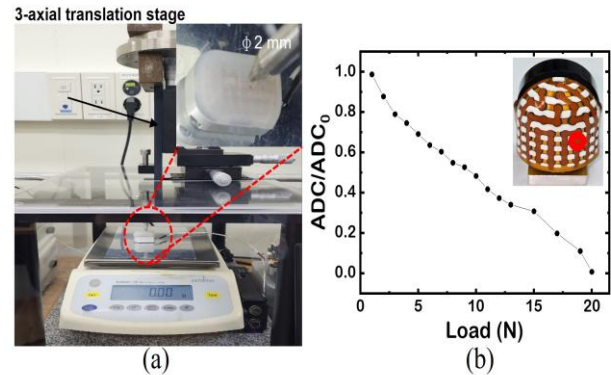
Figure 4. (a) Pressure sensor measurement system.
(b) Detection characteristic of the pressure sensor.
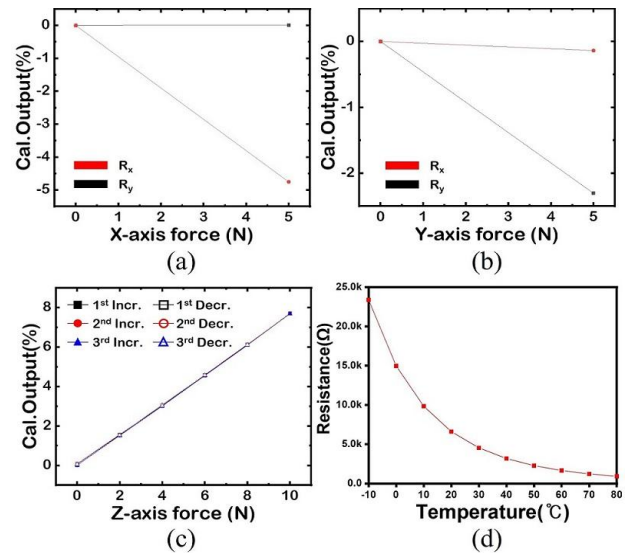
Figure 5. Detection characteristics of a 3-axis force and temperature sensor. (a) Interference characteristics in the X-axis direction. (b) Interference characteristics in the Y-axis direction. (c) Characteristics of repeatability, hysteresis, non-linearity in the Z-axis direction. (d) Detection characteristics of the temperature sensor.

The temperature sensor, a commercial thermistor, demonstrated the capability to detect temperatures within the range of –10 °C to 80 °C (Figure 5 (d)).

IV.   CONCLUSION

We have developed a tactile sensor module for robot fingertips that can be attached to a robot hand. This module is approximately 30 mm × 30 mm × 25 mm in size, tailored

to fit the hand of a commercial robot. The related technologies offer the advantage of customization to accommodate the forms of various robot hands.

The built-in three-axis force sensor has demonstrated reliable results, with low repeatability, hysteresis, and nonlinearity errors, as well as minimal crosstalk between axes. The pressure sensor has achieved high spatial resolution and sensitivity, and the commercial thermistor-based temperature sensor stably detects a wide temperature range.

A comprehensive evaluation of the robot fingertip tactile sensor module confirmed its performance and reliability, meeting the requirements for accurate tactile feedback. Currently, the module is designed to be mounted on the Allegro Hand by Wonik Robotics, and it is being tested in various applications to assess the durability of the module and the performance of each sensor.

In future studies, we aim to address current issues, further miniaturize the module, improve sensor accuracy, and explore additional sensory capabilities to expand the module's functionality.

REFERENCES

[1] J. Dargahi and S. Najarian, "Human tactile perception as a standard for artificial tactile sensing-a review," in Int J Medical Robotics and Computer Assisted Surgery, no. 1, vol. 1, pp. 23-35, 2004.

[2] R. S. Johansson and A. B. Vallbo, "Tactile sensibility in the human hand: Relative and absolute densities of four types of mechanoreceptive units in glabrous skin," in J. Physiol. 1979, 286, pp. 283-300.

Development of an Artificial Fingertip with a High-Sensitivity 3-Axis Force Tactile Sensor Embedded for Robotic Hands

Bo-Gyu Bok
Convergence Research Center for
Meta-Touch
Korea Research Institute of Standards
and Science
Daejeon, Republic of Korea
e-mail: wcsp@kriss.re.kr

Jin-Seok Jang
Convergence Research Center for
Meta-Touch
Korea Research Institute of Standards
and Science
Daejeon, Republic of Korea
e-mail: jang82@kriss.re.kr

Min-Seok Kim
Convergence Research Center for
Meta-Touch
Korea Research Institute of Standards
and Science
Daejeon, Republic of Korea
e-mail: minsk@kriss.re.kr

Abstract— **Advanced robotics engineering, which is gaining attention as a solution to the decline in the labor force, still faces a major challenge due to its immature object manipulation capabilities. Hence, our research team introduces an artificial robotic fingertip equipped with a highly sensitive tri-axial force tactile sensor, designed to enhance the object manipulation capabilities of robots. The tri-axial force sensor array embedded in the fingertip features a hybrid structure that combines the high sensitivity of single-crystal silicon with the excellent mechanical properties of polymer-based rubber. Through a series of evaluations, the developed sensor demonstrated linear output within a measurable range (~1.2 N), high sensitivity, and outstanding fundamental characteristics, such as low hysteresis and repeatability errors. Furthermore, it exhibited the ability to detect forces along each of the three axes independently, without mutual interference.**

Keywords-tactile sensor; dexterous manipulation; robotic hand.

I. INTRODUCTION

Gerontechnology is a portmanteau of "gerontology" and "technology," referring to technologies that address the societal issue of aging populations in modern society [1]. Representative examples include healthcare, advanced robotics engineering, and the Internet of Things (IoT). In particular, research on developing service robots that can ultimately perform tasks on behalf of people is drawing significant interest. However, current robots are limited to performing monotonous tasks like object delivery due to their inadequate object manipulation abilities. In contrast, humans can delicately manipulate objects, detecting slips and preventing them from falling, and even peel tender objects like grapes. This ability arises because, unlike robots that rely solely on vision, humans simultaneously utilize tactile sensation, allowing them to detect various physical quantities generated by the movement of objects in contact with the skin, in addition to vision. Thus, significant research is being conducted to develop tactile sensors that mimic human tactile sensing capabilities, with the aim of enhancing the object manipulation abilities of robots. However, there are still challenges in developing tactile sensors that meet all the requirements (such as high sensitivity, excellent durability,
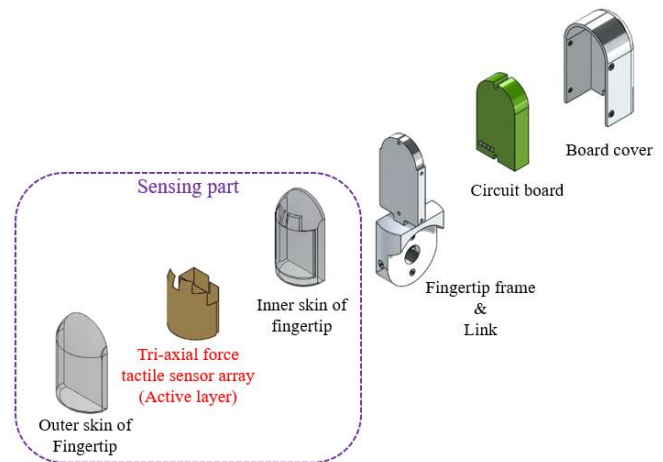
Figure 1. 3D Exploded view of the designed artificial robot fingertip.

low hysteresis error, etc.) [2]. Therefore, our research team would like to propose a highly sensitive tri-axial force tactile sensor array applicable to an artificial fingertip by merging the excellent sensing capabilities of silicon-based strain gauges with the superb mechanical properties of polymer-based rubber. The rest of the paper is organized as follows: In Section II, we present the design and fabrication process of the device. In Section III, we present the results from the sensor evaluation, and finally, we conclude the paper in Section IV.

II. DESIGN & FABRICATION

We designed an artificial fingertip with a highly sensitive tri-axial force sensor array based on the strain gauge. The fingertip comprises a sensing part at the front and a circuit board at the back, centered around the fingertip frame, as detailed in Figure 1. The sensing part consists of a tri-axial force sensor array (active layer) and the inner and outer skin of the fingertip. The tri-axial force sensor array is composed of 12 cells (48 gauges), each comprising four U-shaped strain gauges based on single-crystal silicon nanomembranes. As illustrated in Figure 2, to ensure detection of the tri-axial force distribution across the entire fingertip area, the 12 cells were strategically positioned. The inner skin of the fingertip is positioned beneath the tri-axial force sensor array to

Figure 2. (a) CAD drawing of a tri-axial force tactile sensor array (b) Picture of the circuit board for embedding an artificial fingertip (c) Photograph of the artificial fingertip integrating core technologies.

induce mechanical deformation of the active layer in response to external forces, resulting in resistance changes in the strain gauges. As such, PDMS (Polydimethylsiloxane), which has exc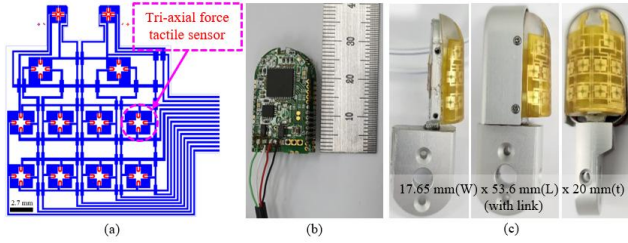ellent deformation properties under external forces, was used, and the inner skin was fabricated using a 10:1 (base: curing agent) mixing ratio of PDMS. Considering the assembly process, the outer skin is designed with 10:1 PDMS for ease of integration with the inner skin. As a result, we devised an artificial fingertip with a highly sensitive three-axis force sensor array based on the sensing part that can have both the high-sensitivity characteristics of single-crystal silicon and the mechanical flexibility of PDMS. To accommodate the circuit board within the robot's fingertip, which is similar in size to a human finger, it was designed with a two-layer structure and was developed to process the signals of 48 strain gauges through a zero-potential method using a DC source. The dimension of the circuit board is 17 mm (W) x 25 mm (H) x 8 mm (t). The fabrication process of the artificial fingertip consists of a process for manufacturing the sensing part through MEMS processes for the production of the active layer and casting processes for the PDMS layers, and an integration process for assembling the manufactured sensing part and a circuit board. Based on processes established in previous research [3], the active layer and PDMS layers were fabricated. The circuit board and fabricated artificial fingertip are shown in Figure 2.

III. EVALUATION

To evaluate the sensing capability of the sensor, the artificial fingertip embedded with the tri-axial force sensor array was positioned on a tri-axial force measurement stage [4]. A metal tip with a diameter of 1 mm was aligned with the center of a single cell, and the changes in gauge output were analyzed as the metal tip was lowered in the vertical direction to measure the normal force sensing characteristics of the sensor. The results showed linear output characteristics within a range of 1.2 N, and superb sensitivity sufficient to detect forces as low as 10 mN. Furthermore, by incrementally increasing and decreasing the load by 0.2 N in each step within the linear output range, the sensor exhibited less than 3% hysteresis error. Also, repeatability error was less than 3% based on 1000 repeated measurements at each step. Next, to evaluate the sensor's performance in detecting shear forces, the output characteristics of the sensor were analyzed as the tip was moved in the X-axis direction by 10 µm increments with a pre-load of 0.15 N applied to a single
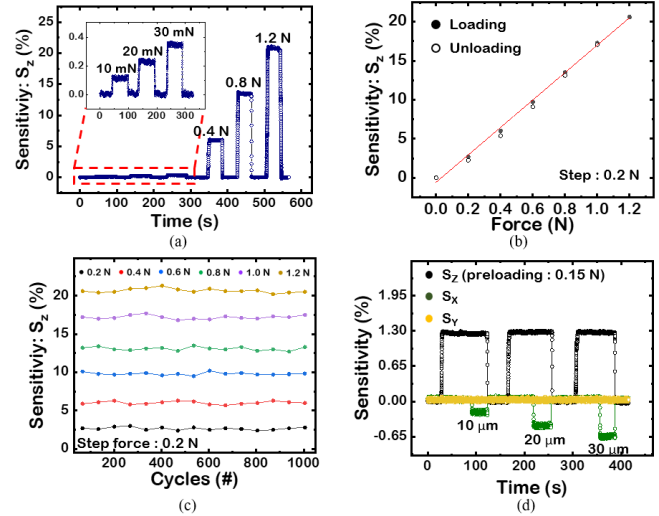
Fig 3. Mechanical characteristics of the tri-axial force tactile sensor array (a) Sensing range & resolution (b) Hysteresis characteristics (c) Repeatability data (d) Tri-axial force output.

cell. As a result, the output of the forces in the Z- and Y-axis directions showed little change, and the cross-talk error, an associated indicator, was less than 3%. Mechanical characteristics of the sensor are shown in Figure 3, and the calculation equations for analyzing the output characteristics of the gauge are presented in previous studies [3][4].

IV. CONCLUSION

Our research team has introduced a highly sensitive tri-axial force tactile sensor array composed of 12 cells that can be embedded in the anthropomorphic fingertip. The tactile sensor showed nearly linear output characteristics for the normal force of 1.2 N or less and was sensitive enough to distinguish the load of 0.1 mN. The hysteresis and repeatability characteristics, fundamental sensing characteristics of the device, exhibited errors of less than 3%. It was demonstrated that forces along tri-axial directions could be detected independently, without mutual interference. In the near future, we plan to conduct experiments to verify whether our anthropomorphic fingertips integrated into a robotic hand can detect the tri-axial force distribution generated by objects when manipulating them in various grasping states. Furthermore, by developing a large-area sensor that can be applied to the entire robot hand, we intend to implement an intelligent robot hand with tactile sensing capabilities similar to human hands.

REFERENCES

[1] P. Sale, Gerontechnology, domotics, and robotics. In Rehabilitation Medicine for Elderly Patients; Springer: Berlin/Heidelberg, Germany, pp. 161–169, 2018.

[2] R. S. Dahiya, G. Metta, M. Valle, and G. Sandini, "Tactile sensing—From humans to humanoids," IEEE Trans. Robot., vol. 26, no. 1, pp. 1–20, Feb. 2010.

[3] B. G. Bok, J. S. Jang, and M.S. Kim. "A highly sensitive multimodal tactile sensing module with planar structure for dexterous manipulation of robots." Adv. Intell. Syst. vol. 5, no. 6, 2200381, Jun. 2023, doi:10.1002/aisy.202200381

[4] M. S. Kim, H. J. Shin, and Y. K. Park, "Design concept of high performance flexible tactile sensors with a robust structure," Int. J. Precis. Eng. Manuf., vol. 13, no. 11, pp. 1941-1947, Oct. 2012.

Comparison of Poole-Frenkel and Hartke Emission Currents in a Capacitive Micromachined Ultrasonic Transducer (CMUT)

Chukwuebuka Okoro, Sazzadur Chowdhury

Department of Electrical and Computer Engineering
University of Windsor
Windsor, Ontario, Canada
e-mail: okoro3@uwindsor.ca

Abstract— **This study investigates the Poole-Frenkel and 3D Hartke models of electron emission from trap centers in silicon nitride membranes in Capacitive Micromachined Ultrasonic Transducers (CMUTs). The study compared the trap-emitted electron current densities calculated using both models for a CMUT, with a 0.5 micrometer thick silicon nitride structural layer suspended over a 600 nanometer thick vacuum gap. The comparison results demonstrate that the Poole-Frenkel model consistently predicts electronic current densities that exceed the Hartke model predictions by more than 99% for a DC bias voltage range of 11-77 volts. This significant variation in predicted current densities is primarily due to the inclusion of multi-directional emission paths in the Hartke model. In contrast, the Poole-Frenkel model considers emissions only in one direction. The study provides valuable insights into the dielectric charging mechanisms in CMUTs, which can aid in the development of solutions to enhance their reliability.**

Keywords- Quantum Tunneling; Current Density; Hartke; Poole-Frenkel; CMUT; Dielectric Charging.

I. INTRODUCTION

Capacitive Micromachined Ultrasonic Transducers (CMUTs) are reciprocal electrostatic transducers that rely on electrostatic or acoustic vibration of a thin suspended membrane to transmit or receive ultrasound [1]. Experimental results established that the CMUTs offer excellent high-quality high-resolution acoustic data collection capabilities that are not possible with conventional piezoelectric transducers [2]-[3]. As the CMUTs and microelectronic Integrated Circuits (ICs) are made using similar microfabrication processes, the CMUTs can easily be integrated with microelectronic ICs to realize 3D-integrated ultrasound microsystems. Such microsystems, by incorporating both the transducers and processing electronics in a System-In-Package (SIP), can offer superior performance with a better Signal-to-Noise Ratio (SNR).

However, it has been observed that during operation, electrical charge accumulation occurs in the dielectric materials used to realize a CMUT geometry. The phenomenon, known as 'dielectric charging', forces a dynamic shift of the CMUT operating point, causing a drift of the CMUT resonant frequency to affect the vibrational characteristics, output pressure, array operation, and reduced receiving sensitivity [4][5]–[8]. Furthermore, a shift in the electric field due to charge accumulation alters the electromechanical coupling coefficient of a CMUT. In [9]-[11], it was mentioned that the CMUT reliability issue due to the dielectric charging phenomenon must be resolved for mainstream adoption of CMUTs for medical and Non-Destructive Evaluation (NDE) applications.

The primary cause of dielectric charging in CMUTs is widely attributed to trap-assisted [4] and quantum tunneling mechanisms [5][6]. Among these, the Poole-Frenkel (PF) emission and Hartke models provide two distinct theoretical frameworks for describing charge transport in the presence of localized trap states. Silicon nitride, a common dielectric material used to fabricate CMUT membranes, inherently contains structural defects, known as K-center traps [7]. These defects arise during thinfilm deposition processes or from high electric field-induced stress, and they act as charge-trapping sites capable of capturing electrons or holes. Under a strong electric field, these trapped charges can be thermally or field-activated to escape into the conduction band, a process known as field-enhanced thermal emission or the Poole-Frenkel (PF) effect.

In the one-dimensional PF model, the applied electric field reduces the Coulombic potential barrier of the trap, thereby enhancing the likelihood of charge emission along the field direction [8]. However, this model simplifies the potential landscape and does not account for multi-directional emission paths.

The Hartke model extends this concept into three dimensions by averaging the field-lowered barrier over all possible emission angles, thereby offering a more accurate depiction of emission behavior in real materials. This is particularly significant at submicron dielectric thicknesses, which are typical in CMUTs, where charge injection and release occur over a distributed field profile [12].

In this context, this paper compares the values predicted by both the PF and Hartke models in the context of CMUTs. The comparison results can be used for more accurate design of CMUTs to improve their reliability by decreasing the dielectric charging effects.

The remainder of this paper is structured as follows: Section II outlines the theoretical models governing field-induced barrier lowering and electron emission in CMUTs, Section III details the MATLAB-based simulations and provides a comparative analysis of the models, the results and their implications are discussed in Section IV, and finally Section V provides the concluding remarks.

II. CMUT DIELECTRIC CHARGING MODELS

The CMUT is essentially a reciprocal electrostatic transducer that functions as a variable capacitor. Figure 1 shows a typical CMUT geometry, which is constructed to have a dielectric spacer enclosed vacuum or air-filled cavity separating a fixed-edge vibrating membrane and a backplate. In the transmit mode, an AC voltage of desired frequency and amplitude, superposed with a suitable DC bias voltage, is applied across the CMUT electrodes as shown in Figure 1. The resulting time-varying electrostatic attraction force between the CMUT electrodes (top membrane and the fixed backplate) causes the membrane to vibrate and generate ultrasound waves in the medium.

During the receive mode, an incident ultrasound wave forces the membrane to vibrate at the incident wave's frequency. This vibration of the membrane dynamically changes the gap between the membrane and the backplate to affect a change in CMUT capacitance. The capacitance change is converted to an output voltage using a suitable microelectronic circuit and a DC bias. Detailed modeling and operating principles of CMUTs are available in [1][2].

In typical fabrication, full or partial metal-coated silicon or silicon nitride films are used to create the CMUT membranes. Wet, dry or low-temperature silicon dioxide (LTO), and in some designs, the buried oxide layer in silicon-on-insulator (SOI) wafers is used to create the dielectric spacer. Silicon nitride has also been used as dielectric spacers in some cases. Often, an insulating layer on the top of the backplate is used to prevent device damage during membrane collapse.

A. Field-Induced Barrier Lowering

Figure 2 shows the potential energy distribution in a typical field emission system comprised of a metal electrode and an insulator. In Figure 2, E_{FM} is the metal Fermi level, W is the metal work function, χ is the insulator electron affinity, $\vec{E}$ is the applied electric field, d is the insulator thickness, ϕ_B is the potential barrier height, $\Delta\phi_B$ is the electric field induced decrease in potential barrier height, and $\psi(x)$ is the effective potential barrier as a function of distance from the metal surface positioned at the origin (x =0). Following Figure 2, the potential barrier $\psi(x)$ can be expressed as

$$\psi(x) = \begin{cases} 0 & x < 0 \\ V_0 - \chi - q\vec{E}_{diel}x & 0 \le x < d \\ V_0 + q(\vec{E} - \vec{E}_{diel})d - q\vec{E}x & x \ge d \end{cases} \quad (1)$$

where $V_0 = W + E_{FM}$. Due to this barrier lowering as expressed in (1), the charges need a smaller energy to escape from the potential wells (traps) in the insulator. As the trapped charges escape, they contribute to a leakage current and exacerbate dielectric charging, ultimately leading to performance degradation and reliability issues in CMUTs

[7]. A conceptual depiction of this barrier lowering in the context of a CMUT is shown in Figure 3. In Figure 3, the field emission occurs from the top metal electrode surface. As in Figure 2, the interface between the metal and the insulator (Si_3N_4 structural layer of the CMUT membrane) is
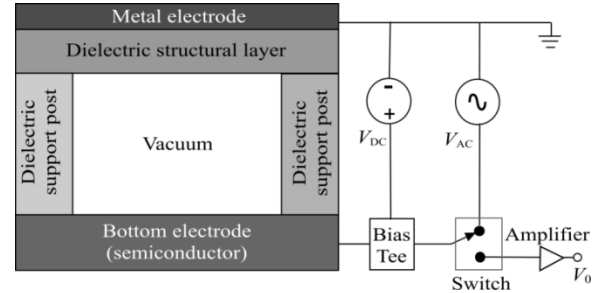
Figure 1. A typical CMUT geometry in an operational setup.

positioned at $x = 0$ and d depicts the thickness of the Si_3N_4 layer. The metal (typically gold) is characterized by a Fermi level E_{FM} and work function W. As in Figure 2, χ is the electron affinity of the Si_3N_4 layer, and E is the initial longitudinal energy of an electron released from a trap in the nitride layer. As Figure 3 shows, the CMUT bias voltage V_{DC} creates an external electric field $\vec{E}$ across the vacuum gap and an electric field $\vec{E}_{diel}$ across the Si_3N_4 layer, reducing the potential energy barrier in both regions.

B. Poole-Frenkel Emission in CMUTs

The PF emission model assumes that the potential barrier lowering caused by an applied electric field occurs only in one direction [13]. For the CMUT geometry in Figure 3, the PF emission model predicted current density J_{PF} can be calculated from [9][14]:

Figure 2. Schematic diagram of a trap center state of an electron showing the conceptual electron emission due to the applied electric field.

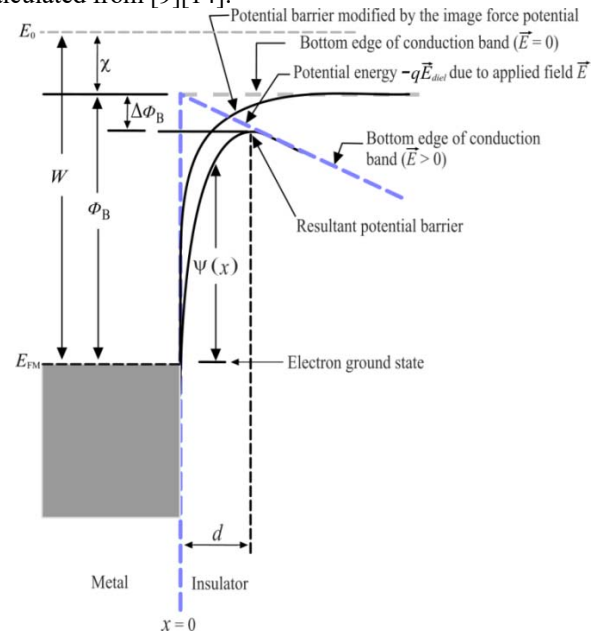$$\left.\begin{aligned} J_{\mathrm{PF}} &= C\vec{E}\exp\left(\frac{-\left(\phi-\beta_{\mathrm{pf}}\sqrt{\vec{E}}\right)}{kT}\right) \\ \beta_{\mathrm{PF}} &= \sqrt{\frac{q^3}{\pi\varepsilon_0\varepsilon_{\mathrm{r}}}} \end{aligned}\right\} \quad (2)$$

In (2), the parameter ϕ is the energy level of the charge trap [15]; C is a pre-exponential factor reported as 0.1 A/V-m for Si_3N_4 [16]; β_{PF} is the PF potential barrier lowering coefficient; ε_0 is the permittivity of free space, ε_{r} is the relative permittivity of the nitride layer; q is the electronic charge; k is the Boltzmann constant and T is the temperature in kelvin.

C. Hartke Emission in CMUTs

Unlike the one-dimensional (1D) PF emission model, the three-dimensional (3D) Hartke emission model incorporates the effect of an applied electric field in a 3D space surrounding the trap centers to characterize the lowering of the potential barrier.

The Hartke model captures this 3D interaction of the electric field with a trap center by introducing angular dependencies where the barrier lowering varies with the angle θ between the direction of the applied field and the emission path, described as $\Delta\phi_{\mathrm{PF}}\cos\theta$ [13]. When this barrier lowering relationship is integrated over all possible emission angles, the effective average barrier lowering is obtained. Following the Hartke model [12][13], the emission current density J_{H} resulting from the electric field $\vec{E}$ associated with the CMUT bias voltage can be
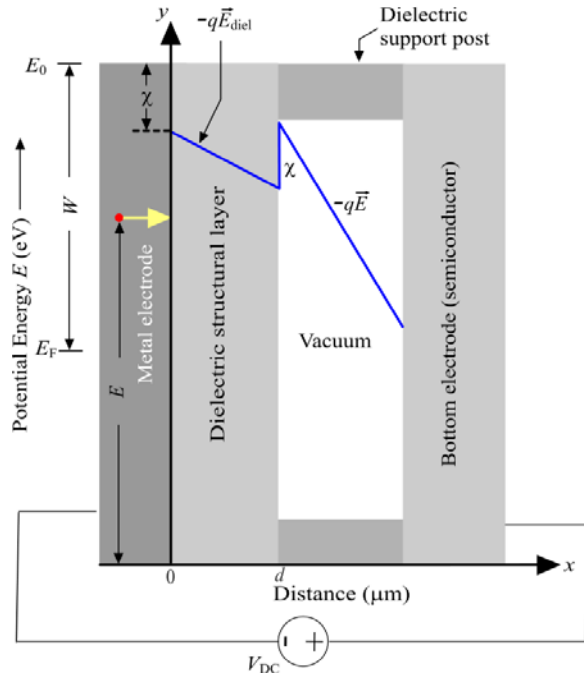

Figure 3. CMUT model showing the triangular barrier lowering due to applied potential energy.

calculated from

$$J_{\mathrm{H}} = \exp\left(\frac{-\phi}{kT}\right)\left(\frac{kT}{\beta\sqrt{E}}\right)^2\left[1+\left(\left(\frac{\beta\sqrt{E}}{kT}\right)-1\right)\exp\left(\frac{\beta\sqrt{E}}{kT}\right)\right]+\frac{1}{2} \quad (3)$$

where the barrier lowering coefficient β and ϕ remains the same as in (2).

It has been observed that this effective average barrier lowering as predicted by the Hartke model is less than the maximum values predicted by the 1D PF emission model [12][13]. This discrepancy, which has its root in the fundamental characterization of the physical phenomenon of charge emission in nitride trap levels, contribute to inaccurate estimation of CMUT leakage currents, which is a major source of dielectric charging in a CMUT.

III. RESULTS

Matlab simulations were conducted to compare the 1D PF model with the 3D Hartke model for a CMUT with specifications and operating conditions as listed in Table 1.

TABLE I. CMUT SPECIFICATIONS.

Parameters	Dimension	Unit
Top electrode thickness (gold)	0.4	µm
Silicon nitride (Si_3N_4) structural layer thickness	0.5	µm
Vacuum gap thickness	0.6	µm
Bottom electrode thickness (silicon)	0.5	µm
Gap between electrodes	1.1	µm
Temperature	300	K

Figure 4 shows the PF current density J_{PF} as a function of the electric field $\vec{E}$ due to the bias voltage V_{DC} applied to a CMUT with specifications as listed in Table I. As Figure 4 reveals, the PF current density J_{PF} increases rapidly as the effective barrier height decreases with an increasing electric field associated with the 11-77 volts bias voltage range. Similarly, Figure 5 shows the Hartke model predicted
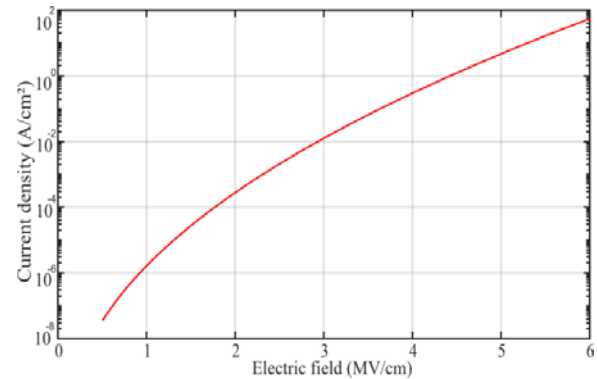

Figure 4. PF model predicted current density due to the trap centers in the CMUT silicon nitride membrane as a function of the lectric field associated with the CMUT bias voltage.
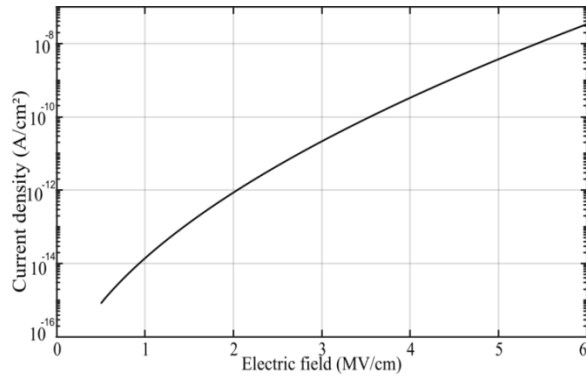
Figure 5.   3D Hartke model predicted current density due to the trap centers in the CMUT silicon nitride membrane as a function of the electric field associated with the CMUT bias voltage.
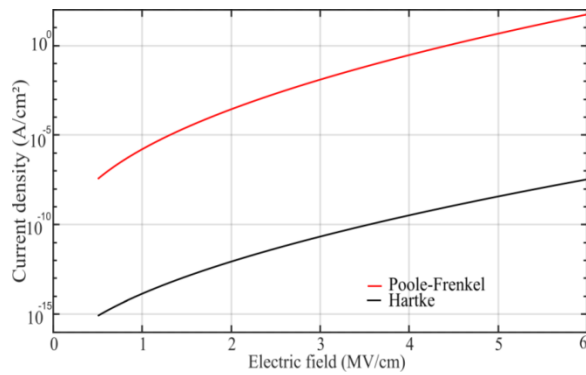

Figure 6.   Current density at 300K for Hartke and PF emission models.

TABLE II.   CURRENT DENSITY COMPARISON.

Bias Voltage (V)	Hartke model current density, J_H (A/cm^2)	Poole-Frenkel model current density J_{PF} (A/cm^2)	$\Delta\%$ $\frac{J_{PF} - J_H}{J_{PF}} \times 100$
11	2.689×10^{-12}	1.077×10^{-10}	97.5
22	8.154×10^{-12}	8.771×10^{-10}	99.0
33	2.016×10^{-11}	3.864×10^{-9}	99.47
44	4.425×10^{-11}	1.277×10^{-8}	99.65
55	8.950×10^{-11}	3.555×10^{-8}	99.83
66	1.704×10^{-10}	8.796×10^{-8}	99.80
77	3.099×10^{-10}	1.996×10^{-7}	99.84

current density J_H as a function of the electric field $\vec{E}$ associated with the same CMUT after applying the same bias voltage. As expected, the Hartke model predicted current density also increases rapidly with an increasing electric field. Figure 6 compares the current densities predicted by both models for the same CMUT geometry subject to the same electric field variations. The percent variations ($\Delta\%$) in the current densities predicted by both the models are tabulated in Table II. As Table II shows, the PF model predicted current density consistently predicts higher current densities compared to the Hartke model by more than 99% for the used bias voltage range.

IV.   DISCUSSIONS

Figure 6 and Table II clearly establish that the Hartke model predicted values are order of magnitude smaller than those predicted by the widely used Pool-Frenkel model for the same bias voltage. The reason for this deviation apparently appears to be the directional interaction of the applied electric field with the trap geometry, which is basically a 3D potential well.

The PF model approximates this interaction using a one-directional approach, while the Hartke model considers the 3D nature of the trap. It is therefore safer to conclude that the 3D Hartke model is more realistic for predicting the current density in the silicon nitride membrane of a CMUT.

The trap density in a silicon nitride layer is influenced by the specific composition of silicon and nitrogen within the layer. The parameters of the deposition process, such as plasma-enhanced chemical vapor deposition (PECVD) or low-pressure chemical vapor deposition (LPCVD), greatly influence the composition of the deposited materials in a thin film. It is worth examining the electron trap current densities as a function of both silicon and nitrogen composition in the silicon nitride layer. To carry out this investigation, three different layers of silicon nitride were utilized, each with varying compositions of silicon and nitrogen as listed in Table III [17]. Table III illustrates that there is a direct relationship between the nitrogen content in silicon nitride and the energy trap depth. As the nitrogen content increases, the energy trap depth also increases. Figure 7 shows the corresponding electron current densities, calculated using the Hartke model, plotted as a function of the applied electric field. Figure 7 illustrates that among the 3 investigated silicon nitride layers, the one with the lowest nitrogen concentration (and therefore the lowest energy trap depth of 0.56 eV) results in the highest emission current density at the same electric field strength.

V.   CONCLUSION AND FUTURE WORK

The electron current densities resulting from electron emissions from trap centers in microfabricated silicon nitride membranes of CMUTs were examined using both the 1D PF model and the 3D Hartke model. The investigation revealed that the PF model consistently predicts emission current densities that are more than 99% higher than those predicted by the Hartke model within the bias voltage range of 11-77 volts. To provide context, a theoretical study published in [18] concluded that the 1D PF model consistently predicted a 66% higher emission rate compared to the 3D Hartke model for two plane parallel electrodes separated by a dielectric. Obviously, the PF model overestimates the emission current.

TABLE III.   DIFFERENT SILICON NITRIDE COMPOSITIONS WITH CORRESPONDING TRAP DEPTHS

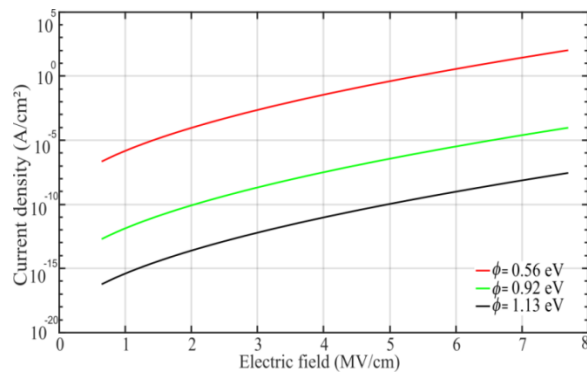| Composition	Trap depth/ionization potential ϕ (eV)
$SiN_{0.75}$	0.56
$SiN_{1.17}$	0.92
$SiN_{1.22}$	1.13

Figure 7.   The Hartke model predicted current densities for three different silicon nitride layers with varying composition of silicon and nitrogen and trap depth energy levels as listed in Table III.

Apparently, this is due to its assumption of a one-dimensional potential barrier lowering. However, the Hartke model, which takes into account the three-dimensional behavior of traps, aligns more closely with actual trap behavior. It can be concluded that, in comparison to the PF model, the Hartke model is a more accurate method for predicting the emission current in 3D microstructures, such as a CMUT that uses a vibrating silicon nitride membrane to transmit or receive ultrasound.

Furthermore, during vibration, the silicon nitride membrane of a CMUT deforms causing distortion of the energy levels of the charge traps located within the membrane. It is thus necessary to evaluate the Hartke model predicted current densities in dynamically vibrating CMUT membranes against experimentally measured values.

REFERENCES

[1] J. Jayapandian, K. Prabakar, C. Sundar, and B. Raj, "On the Design, Fabrication, and Characterization of cMUT Devices," in Materials and Failures in MEMS and NEMS, 1st ed., A. Tiwari and B. Raj, Eds., Wiley, 2015, pp. 201–218. doi: 10.1002/9781119083887.ch6.

[2] P. Zhang, G. Fitzpatrick, W. Moussa, and R. Zemp, "CMUTs with improved electrical safety & minimal dielectric surface charging," in Proc. 2010 IEEE International Ultrasonics Symposium, San Diego, CA, USA: IEEE, Oct. 2010, pp. 1881–1885. doi: 10.1109/ULTSYM.2010.5935744.

[3] N. Tavassolian, "Dielectric charging in capacitive RF MEMS switches with silicon nitride and silicon dioxide," PhD Dissertation, Georgia Institute of Technology, 2011.

[4] X. Zhang, H. Zhang, and D. Li, "Design of a hexagonal air-coupled capacitive micromachined ultrasonic transducer for air parametric array," Nanotechnology and Precision Engineering, vol. 4, no. 1, p. 013004, Mar. 2021, doi: 10.1063/10.0003504.

[5] S. Machida, T. Takezaki, T. Kobayashi, H. Tanaka, and T. Nagata, "Highly reliable CMUT cell structure with reduced dielectric charging effect," 2015 IEEE International Ultrasonics Symposium (IUS), Taipei, Taiwan, 2015, pp. 1-4, doi: 10.1109/ULTSYM.2015.0061

[6] S. O. Kasap, Principles of electronic materials and devices, Fourth edition. New York, NY: McGraw-Hill, 2018.

[7] X. Yuan, et al, "Initial Observation and Analysis of Dielectric–Charging Effects on RF MEMS Capacitive Switches", in Proc. 2004 IEEE MTT–S International Microwave Symposium Digest, vol. 3, 2004, pp. 1943–1946

[8] H. Wang, Y. Tong, X. Wang, C. He, and C. Xue, "Experimental investigation of the influence of excitation signal on radiation characteristics of capacitive micromachined ultrasonic transducer," Microsyst Technol, vol. 24, no. 12, pp. 5055–5063, Dec. 2018, doi: 10.1007/s00542-018-4131-8.

[9] J. Li, Y. Li, and P. Zhang, "Modelling and Analysis of Dielectric Charge of CMUTs," IOP Conf. Ser.: Mater. Sci. Eng., vol. 768, no. 6, p. 062106, Mar. 2020, doi: 10.1088/1757-899X/768/6/062106.

[10] M. Koutsoureli, D. Birbiliotis, L. Michalas, and G. Papaioannou, "Dielectric charging in MEMS capacitive switches: a persisting reliability issue, available models and assessment methods," in Proc. of 2016 16th Mediterranean Microwave Symposium (MMS), Abu Dhabi, United Arab Emirates: IEEE, Nov. 2016, pp. 1–4. doi: 10.1109/MMS.2016.7803802.

[11] J. Munir, Q. Ain, and H. Lee, "Reliability issue related to dielectric charging in capacitive micromachined ultrasonic transducers: A review," Microelectronics Reliability, vol. 92, pp. 155–167, Jan. 2019, doi: 10.1016/j.microrel.2018.12.005.

[12] J. Hartke, "The Three-Dimensional Poole-Frenkel Effect," Journal of Applied Physics, vol. 39, no. 10, pp. 4871–4873, Sep. 1968, doi: 10.1063/1.1655871.

[13] O. Mitrofanov and M. Manfra, "Poole-Frenkel electron emission from the traps in AlGaN/GaN transistors," Journal of Applied Physics, vol. 95, no. 11, pp. 6414–6419, Jun. 2004, doi: 10.1063/1.1719264.

[14] V. Kapoor and S. Bibyk, "Energy distribution of electron-trapping centers in low-pressure chemically vapor-deposited Si3N4 films," Thin Solid Films, vol. 78, no. 2, pp. 193–201, 1981, doi: https://doi.org/10.1016/0040-6090(81)90619-2.

[15] Y. Zhou and P. Zhang, "Theory of field emission from dielectric coated surfaces," Phys. Rev. Research, vol. 2, no. 4, p. 043439, Dec. 2020, doi: 10.1103/PhysRevResearch 2.043439.

[16] "The Reliability of the Silicon Nitride Dielectric in Capacitive MEMS," Docslib. [Online]. Available: https://docslib.org/doc/505598/the-reliability-of-the-silicon-nitride-dielectric-in-capacitive-mems, Retrieved: Feb., 2025.

[17] R. Apodaca, "Electrical Characterization of Silicon-Rich Nitride and Silicon Oxynitride Films Deposited by Low-Pressure Chemical Vapor Deposition," Master's Thesis, University of New Mexico. Electrical Engineering, 2005.

[18] P. Murgatroyd, "Theory of space-charge-limited current enhanced by Frenkel effect," J. Phys. D: Appl. Phys., vol. 3, no. 2, pp. 151–156, Feb. 1970, doi: 10.1088/0022-3727/3/2/30

Spectral and Angular Analysis of Reflectance in Mobile Robot Prototypes under Controlled Artificial Lighting

Paulo Pimentel Zottino, Andre Schneider de Oliveira ⓘ, and Ronnier Frates Rohrich ⓘ

Graduate Program in Electrical and Computer Engineering

Graduate Program in Computer Science

Universidade Tecnológica Federal do Paraná

Curitiba, Brazil

e-mail:{rohrich}@utfpr.edu.br

Abstract—**Environmental monitoring in sports arenas presents challenges related to light interference in optical sensors. This study experimentally investigated the influence of different color spectra and angles of incidence on light reflection in scaled prototypes of a mobile robot. Polylactic Acid (PLA) was used as the base material for constructing six conceptual models. The analyses considered representative colors from the visible light spectrum (380–750 nm), also including conditions with black light (ultraviolet, outside the visible spectrum) and white light (a combination of the entire visible spectrum). The tests were conducted in a controlled environment, with Light Emitting Diode (LED) lighting and light intensity measured by a lux meter, using a reference baseline of 10.76 lux. The light incidence angles ranged from $30°$ to $120°$. The results showed that the white color exhibited the highest reflectance (MGI: 17.53 lux; +62.92%), with a reflection peak at $30°$ (+150.09%). In contrast, the black color reflected the least amount of light (MGI: 10.46 lux; -2.79%), with the lowest value recorded at $90°$ (-9.94%). Intermediate colors, such as yellow (+27.23%) and orange (+12.92%), showed moderate levels of reflection.**

Keywords-Light reflection; Robotic design; Optical sensors; Environmental monitoring; Sports arenas.

I. INTRODUCTION

Environmental monitoring in sports arenas—such as football fields, gymnasiums, and courts—is essential to ensure appropriate conditions during events, especially in environments with variable light from sunlight or spotlights. Robots equipped with optical sensors have been used to measure temperature, humidity, and air quality, contributing to operational efficiency and safety during large-scale sporting events [1]. However, the interaction between ambient light and robot surfaces presents a challenge: light reflection on chassis materials may interfere with sensor accuracy, resulting in errors in data collection or autonomous navigation. This issue is particularly relevant in sports arenas, where lighting variations influence the choice of materials and designs to reduce interference.

Light reflection on robot surfaces can affect the performance of optical sensors responsible for detecting environmental variables, especially under dynamic lighting conditions. The choice of colors and materials directly impacts reflected illuminance and can compromise data reading accuracy or task execution, such as navigation. This study experimentally analyzes light reflection on conceptual 3D PLA models simulating robots, to assess how color and angle of incidence affect reflected illuminance. Conceptual models were produced in six colors (Yellow, White, Orange, Green, Blue, Black) and tested at seven incidence angles (30° to 120°) inside a dark chamber measuring 60 cm × 26 cm × 20 cm, painted matte black to minimize external reflections. An LED lamp emitted light, and illuminance was measured using a Vonder LDV 2000 lux meter, with a reference baseline of 10.76 lux in the empty chamber. This paper aims to discuss the selection of materials' colors for robot design, seeking to reduce interference and improve sensor efficiency in environmental monitoring within sports arenas. This paper aims to discuss the selection of materials' colors for robot design, seeking to reduce interference and improve sensor efficiency in environmental monitoring within sports arenas. In Section 2, related works are reviewed to provide the theoretical and experimental context of the study. Section 3 introduces the Spectral Analysis System Architecture, describing the experimental setup and measurement procedures. The obtained data and their interpretation are presented in Section 4, Results and Discussion. Finally, Section 5 concludes the paper by summarizing the key findings and outlining directions for future research.

II. RELATED WORK

The use of robots in sports and environmental contexts has gained prominence in the scientific literature. In the sports domain, Siegel and Morris [2] analyzed the impact of automation and robotics on sports, addressing refereeing, field maintenance, and audience experiences, highlighting the potential of robots in sports arenas. Hameed et al. [3] focused on robots for grass cutting and automatic field marking, presenting algorithms for line generation and operational guidance, thus connecting environmental robotics to sports arenas.

In environmental monitoring, Dunbabin and Marques [4] presented advances in robots to monitor terrestrial, aquatic, and aerial environments, emphasizing applications and challenges. Bogue [1] examined the role of robots in environmental monitoring, including drones and ground robots, with applications in data collection and pollution detection. Hegde et al. [5] explored sensors in soft robotics, emphasizing flexibility and the integration of lightweight electronic systems, while Keicher and Seufert [6] analyzed automatic guidance technologies in agricultural vehicles, applicable to robot navigation on sports fields.

Regarding material selection, Ullah and Harib [7] proposed an intelligent method based on performance, cost, and sustainability. Coyle et al. [8] discussed biologically inspired soft robotics, addressing material selection and design, while Hussain et al. [9] reviewed materials and fabrication techniques in robotic exoskeletons. In terms of design, Bechthold and King [10] discussed the integration of robotics into design and architecture, focusing on digital fabrication.

There is a noticeable gap in the literature regarding the experimental analysis of the interaction between light and robotic surfaces in sports contexts. This study investigates how colors and incidence angles affect light reflection on 3D PLA conceptual models, providing insights for more effective robot design in sports arenas.

III. SPECTRAL ANALYSIS SYSTEM ARCHITECTURE

The experimental architecture was developed to evaluate the impact of light reflection on environmental monitoring robots in sports arenas. The *setup* consisted of a dark chamber measuring 60 cm × 26 cm × 20 cm, painted matte black to minimize external reflections, and equipped with a LED lamp (Elgin Smart Color, white mode, 100% intensity) as the light source, as presented in Figure 1. Conceptual robot models, 3D-printed in PLA in six colors (yellow, white, orange, green, blue, and black), were individually placed in the chamber to simulate robotic surfaces. Reflected illuminance was measured using a Vonder LDV 2000 lux meter positioned 35 cm from the conceptual model, with seven incidence angles tested (30° to 120°). Three measurements were taken for each condition, all yielding identical results, confirming experimental stability. The empty chamber established a baseline reference of 10.76 lux.

evaluation. The inner walls were painted matte black and an LED lamp was mounted on the roof as a light source. The conceptual model was placed in the center and the lux meter, placed 13 cm away, to measure the reflected illuminance. The region responsible for data acquisition (part of the sensor) is indicated in Figure 2.
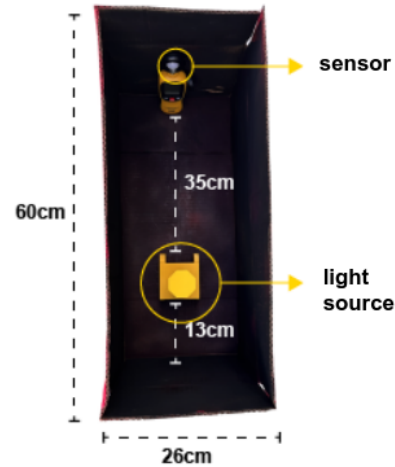

Figure 2. Top view of the dark chamber.

B. Conceptual Models

Six conceptual robot models were 3D printed using polylactic acid (PLA) filament, each with a height of 20 cm, in the colors yellow, white, orange, green, blue and black, as shown in Figure 3.
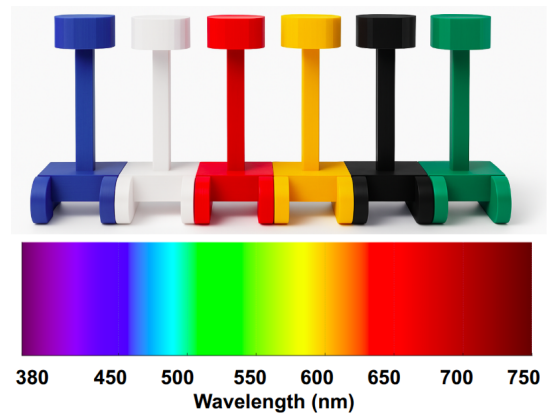

Figure 3. Conceptual models with color labels: Yellow, White, Orange, Green, Blue, Black, and the visible spectrum.

PLA was selected as the base material due to its high market availability, low cost, ease of printing, and good dimensional stability—characteristics that make it widely used in rapid prototyping projects and experimental robot development. Furthermore, as a thermoplastic derived from renewable resources and biodegradable, PLA presents environmental advantages compared to other commonly used materials, such as ABS.

The material has a slightly glossy and homogeneous surface finish, which favors optical reflectance analysis under controlled

Figure 1. General schematic of the experiment, showing the dark chamber with the LED lamp, a conceptual robot model, and the lux meter.

A. Dark Chamber

A dark chamber, with dimensions of 60 cm × 26 cm × 20 cm, was constructed to ensure a controlled environment with standardized lighting for

lighting conditions. The selected colors were carefully chosen to represent different optical behaviors, ranging from light tones, such as white and yellow, which tend to reflect a greater amount of light, to darker tones, such as blue and black, which absorb light more intensely. Intermediate colors, such as green and orange, complete the sample set, enabling comparative analysis of the light response across a representative range of the visible spectrum. This chromatic variety is essential to evaluate the impact of surface color on the efficiency of optical sensors embedded in mobile robots.

Regarding illumination and light reflection, the visible spectrum extends approximately 380 nm to 750 nm. Black light, such as that emitted by ultraviolet lamps, is not part of the visible spectrum and lies in the ultraviolet (UV) range, which includes the following wavelength subcategories:

- UV-A: 315–400 nm;
- UV-B: 280–315 nm;
- UV-C: 100–280 nm.

Thus, from a wavelength perspective, black light falls below 380 nm and is not visible to the human eye. White light, on the other hand, does not have a single wavelength, as it results from the balanced combination of all colors in the visible spectrum. White light spans the entire visible range, from 380 nm to 750 nm. Therefore, white light does not occupy a specific position within the spectrum but is a mixture of multiple visible light frequencies.

C. Light Source and Sensing

The light source used in the experiment was an Elgin Smart Color LED lamp, operating in white mode at 100% intensity, ensuring consistent and controlled illumination. This lamp has a power rating of 10 W and a luminous flux ranging between 800 and 1,000 lumens, providing adequate brightness for testing in controlled environments. This light source was selected based on its ability to deliver efficient and uniform lighting, which is essential for analyzing the reflectance of robotic model surfaces. The white mode was chosen to ensure coverage of the entire visible spectrum, from the shortest wavelengths (violet) to the longest (red), simulating daylight-like illumination and enabling a comprehensive study of light–surface interactions. The lamp was positioned outside the dark chamber to allow light to be directed at the required angles while maintaining an illuminance level of 10.76 lux inside the empty chamber.

Reflected illuminance from the model surfaces was measured using a Vonder LDV 2000 lux meter, a high-precision device that quantifies the luminous intensity reflected by different prototype colors. This lux meter features a measurement range from 0.1 to 200,000 lux, enabling readings across a wide range of lighting conditions, from low-intensity environments to brightly lit scenarios. The device has an accuracy of ±3%, ensuring minimal error in the readings and guaranteeing the reliability of the experimental data. Using this measurement instrument contributes to obtaining consistent and comparable results, which is essential for analyzing the reflectance behavior of different colors and light incidence angles on the conceptual models.

D. Experimental Conditions

The light source was systematically positioned at seven distinct incidence angles (30°, 45°, 60°, 75°, 90°, 105°, and 120°), as illustrated in Figures 4 and 5.
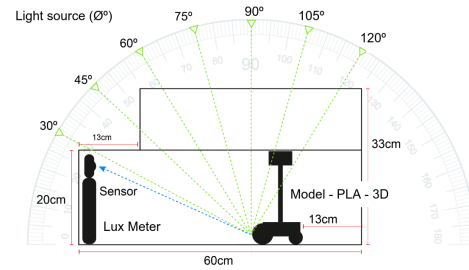

Figure 4. Side view of the dark chamber, showing the angles of incidence.

For each angular configuration, three independent measurements were conducted, all of which demonstrated complete reproducibility of the results.
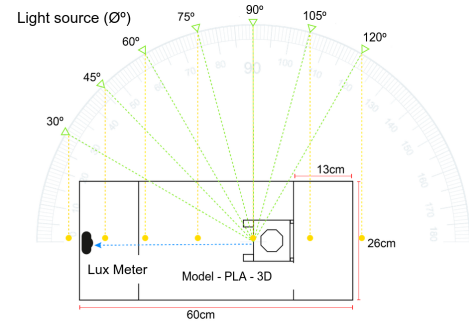

Figure 5. Top view of the dark chamber, with labels: Lamp, conceptual model, Luxmeter; distance from conceptual model to luxmeter: 13 cm.

IV. RESULTS AND DISCUSSION

The experimental results demonstrated clear differences in light reflection across the colors of the conceptual 3D-printed PLA models, as illustrated in Figure 6.
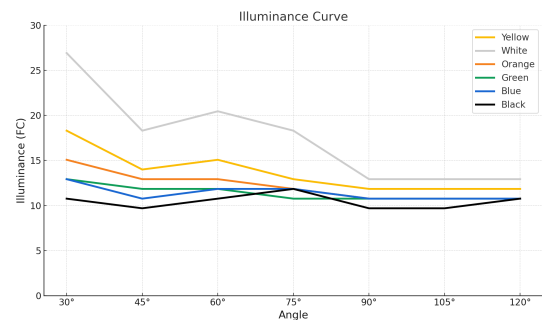

Figure 6. Illuminance curve as a function of the angle of incidence (30° to 120°), with lines representing each color.

The white model presented the highest reflectance, with a General Mean Illuminance (GMI) of 17.53 Lux and a peak of 26.91 Lux at 30°, while the black model exhibited the lowest performance, with a GMI of 10.46 Lux and minimum values of 9.69 Lux at 45°, 90°, and 105°. The other colors

showed intermediate behaviors: yellow (GMI 13.69 Lux), orange (GMI 12.15 Lux), and green and blue (both GMI 11.38 Lux). In practical terms, illuminance consistently varied with the incidence angle, reaching maximum values at 30° and dropping to a minimum at 90°. This angular dependence, summarized in Table I, highlights the importance of material color and geometry in applications where light distribution and efficiency are critical design parameters.

TABLE I. AVERAGE ILLUMINANCE (FC)

	30°	45°	60°	75°	90°	105°	120°	MGI	Notes
EMPTY	10.8	10.8	10.8	10.8	10.8	10.8	10.8	10.8	
YELLOW	18.3	14.0	15.1	13.0	11.9	11.9	11.9	13.7	
WHITE	27.0	18.3	20.5	18.3	12.9	12.9	12.9	17.5	HIGHEST REFLEC.
ORANGE	15.1	12.9	12.9	11.8	10.8	10.8	10.8	12.2	
GREEN	12.9	11.8	11.8	10.8	10.8	10.8	10.8	11.4	
BLUE	12.9	10.8	11.8	11.8	10.8	10.8	10.8	11.4	
BLACK	10.8	9.7	10.8	11.8	9.7	9.7	10.8	10.5	LOWEST REFLEC.

The distribution of reflection values, illustrated in the histogram (Figure) 7, shows a clear trend: light-colored models (white and yellow) reflect significantly more light than darker ones (black, blue, and green), with orange exhibiting intermediate behavior.
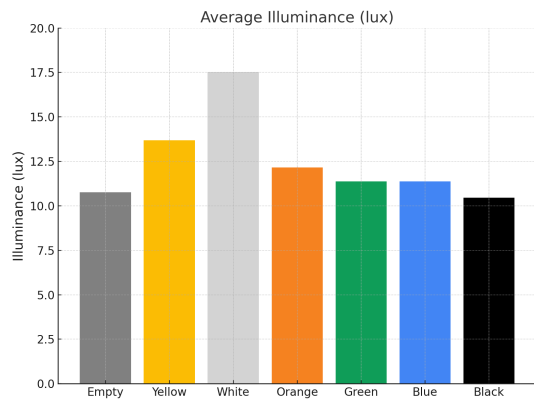

Figure 7. Histogram of overall average illuminance (MGI) by color.

This distinction emphasizes the role of material color in influencing light performance, an important factor when selecting polymers for applications requiring controlled reflection or optimized illumination.

V. CONCLUSION AND FUTURE WORK

This study revealed that light colors, such as White (GMI 17.53 Lux, +62.92% compared to the baseline of 10.76 Lux), reflect more light than dark colors, such as Black (GMI 10.46 Lux, -2.79%), with reflection being more intense at grazing angles (30°, White: +150.09%) and lower at perpendicular angles (90°, Black: -9.94%). Intermediate colors exhibited behavior between these extremes. These findings contribute to the design of robots in sports arenas, indicating that color selection can optimize the accuracy of optical sensors. Future research may explore other materials and natural lighting conditions.

REFERENCES

[1] R. Bogue, "The role of robots in environmental monitoring", *Industrial Robot: the international journal of robotics research and application*, vol. 50, no. 3, pp. 369–375, Jan. 2023, ISSN: 0143-991X.

[2] J. Siegel and D. Morris, "Robotics, automation, and the future of sports", in *21st Century Sports: How Technologies Will Change Sports in the Digital Age*, S. L. Schmidt, Ed. Cham: Springer International Publishing, 2020, pp. 53–72.

[3] I. A. Hameed, C. G. Sorrenson, D. Bochtis, and O. Green, "Field robotics in sports: Automatic generation of guidance lines for automatic grass cutting, striping and pitch marking of football playing fields", *International Journal of Advanced Robotic Systems*, vol. 8, no. 1, p. 10, 2011.

[4] M. Dunbabin and L. Marques, "Robots for environmental monitoring: Significant advancements and applications", *IEEE Robotics Automation Magazine*, vol. 19, no. 1, pp. 24–39, 2012.

[5] C. Hegde et al., "Sensing in soft robotics", *ACS Nano*, vol. 17, no. 16, pp. 15 277–15 307, 2023.

[6] R. Keicher and H. Seufert, "Automatic guidance for agricultural vehicles in europe", *Computers and Electronics in Agriculture*, vol. 25, no. 1, pp. 169–194, 2000, ISSN: 0168-1699.

[7] A. S. Ullah and K. H. Harib, "An intelligent method for selecting optimal materials and its application", *Advanced Engineering Informatics*, vol. 22, no. 4, pp. 473–483, 2008, PLM Challenges, ISSN: 1474-0346.

[8] S. Coyle, C. Majidi, P. LeDuc, and K. J. Hsia, "Bio-inspired soft robotics: Material selection, actuation, and design", *Extreme Mechanics Letters*, vol. 22, pp. 51–59, 2018, ISSN: 2352-4316.

[9] F. Hussain, R. Goecke, and M. Mohammadian, "Exoskeleton robots for lower limb assistance: A review of materials, actuation, and manufacturing methods", *Proceedings of the Institution of Mechanical Engineers, Part H: Journal of Engineering in Medicine*, vol. 235, no. 12, pp. 1375–1385, 2021.

[10] M. Bechthold and N. King, "Design robotics", in *Rob | Arch 2012*, S. Brell-Çokcan and J. Braumann, Eds., Vienna: Springer Vienna, 2013, pp. 118–130.

Performance Evaluation of An Autonomous Time-synchronized Sensing System with A Camera Sensor

Narito Kurata

Faculty of Industrial Technology
Tsukuba University of Technology
Tsukuba City, Ibaraki, Japan
e-mail: kurata@home.email.ne.jp

Abstract - **The maintenance of aging civil infrastructure, such as bridges, highways, and buildings, has become a critical social issue in Japan. Proper maintenance requires regular and highly accurate inspections; however, these inspections still rely heavily on human visual observation, which is costly. To improve efficiency, automated sensing systems are increasingly needed. Moreover, following large-scale disasters such as earthquakes and tsunamis, rapid evacuation and rescue operations must be carried out. For this purpose, it is essential to quickly and accurately evaluate structural integrity and damage using sensing systems. To address these challenges, research and development have been conducted on an autonomous time-synchronized sensing system that assigns highly precise time information to measurement data, enabling synchronized acquisition and analysis across multiple sensors. As an initial step, a sensor device was developed that realizes autonomous time-synchronized sensing using a high-precision digital accelerometer. Subsequently, a heterogeneous digital sensing platform was prototyped, allowing simultaneous connection of both a digital accelerometer and a camera sensor. In this system, accelerometer data and camera images are assigned unified timestamps synchronized with absolute time at the instant of acquisition. This enables synchronized measurement of vibration and imagery. The timestamping mechanism relies on the accuracy of a Chip-Scale Atomic Clock (CSAC) mounted on the device. Experimental evaluation confirmed that the prototype system achieves the desired performance. This paper describes the details of the time synchronization mechanism using a CSAC and presents detailed experimental results regarding its performance.**

Keywords-Time Synchronization; Chip Scale Atomic Clock; Earthquake Observation; Structural Health Monitoring; Micro Electro Mechanical Systems; Camera Sensor

I. INTRODUCTION

Civil infrastructure such as bridges, highways, and high-rise buildings deteriorates with time, and automation of inspection for their maintenance and management has become an important social issue. In Japan, which is prone to earthquakes and other disasters, rapid post-disaster detection of structural damage and evaluation of its extent are required. Automated inspections and damage detection require data collection using sensing systems. To analyze data measured by multiple sensors and evaluate structural integrity, time synchronization among sensors is essential. Without synchronized data, cross-sensor and time-series analyses that use phase information cannot be performed. Time synchronization methods have traditionally been implemented using dedicated wiring, wired networks, or wireless networks. However, wired synchronization imposes significant restrictions on sensor placement, whereas wireless synchronization is applicable only where wireless communication between sensors is possible. In either case, wide-area deployment is infeasible. Conversely, if sensors installed at arbitrary locations can autonomously maintain accurate time information, this issue can be overcome. The Global Positioning System (GPS) is effective for outdoor synchronization but is unusable indoors, underground, beneath bridges, or in tunnels. To overcome this limitation, a sensor device capable of autonomously maintaining precise time information was developed using a chip-scale atomic clock (CSAC) [1][2][3][7], an ultra-high-precision clock [4][8][9]. For earthquake observation, logic was implemented to detect earthquakes and record seismic event data, and its functionality was validated using shaking-table experiments. The developed sensor device was also deployed in actual buildings and bridges for earthquake observation and structural health monitoring [4]. However, the device initially employed a MEMS accelerometer, which struggled to measure minute vibrations accurately and remained susceptible to analog-signal noise contamination. Therefore, the accelerometer was replaced with a digital type, eliminating the risk of noise [5]. A camera sensor was also integrated, and a heterogeneous digital sensing platform was prototyped [6]. A previous paper described the design and construction of the autonomous time-synchronized sensing system based on prior research and development, including a mechanism to append ultra-precise time information to sensor data using the CSAC [1]. In this paper, the details of the time synchronization mechanism using the CSAC and experimental results on the time-synchronization performance of the developed sensing system are presented. Section II reviews existing time synchronization methods, their limitations, and the achievements of the proposed digital sensing platform. Section III describes the overview of the developed sensor device and the time synchronization mechanism using the CSAC. Section IV provides details of the performance verification experiments on synchronizing the camera sensor and external input sensors. Finally, Section V presents the conclusions and future work.

II. STATE OF THE ART

Research on time synchronization in sensing systems has been extensive, including the use of Global Navigation Satellite System (GNSS) signals via satellites [12] and the Network Time Protocol (NTP) [10] for synchronization on the Internet. Other studies have explored synchronization in wireless sensor networks, leveraging low propagation delay. For example, protocols such as Reference Broadcast Synchronization [13], Timing-sync Protocol for Sensor Networks [14], and the Flooding Time Synchronization Protocol [11] have been proposed. While wireless-based methods are convenient, they cannot guarantee reliable communication. In particular, during disasters such as earthquakes, wireless communication may be disrupted, rendering time-synchronized sensing and data analysis infeasible. The IEEE 1588 Precision Time Protocol (PTP) achieves high-accuracy synchronization indoors by using Ethernet cables as transmission paths in general Local Area Networks (LANs). PTP can provide synchronization accuracy within 1 microsecond. However, maintaining stable accuracy is difficult due to fluctuations in packet delays and packet losses caused by congestion. Furthermore, because synchronization relies on packet switching compensation, the number of devices that can be connected to the master is limited, and wide-area deployment is impractical.

When GPS signals are unavailable, wireless connections unstable, and wired networks inaccessible, it is desirable for sensors to autonomously maintain precise absolute time information. If each sensor can append accurate timestamps to its measured data, autonomous time-synchronized data collection becomes possible. To realize this, a sensor device was developed using a CSAC [2][3][7]. CSAC provides ultra-high-accuracy time measurement (on the order of tens of picoseconds, 5×10^{-11} s) while being sufficiently compact for board mounting. Development began in 2001 with support from DARPA, and consumer versions were released in 2011 [9]. CSACs are expected to be further miniaturized and reduced in cost as their applications expand, including GPS interference countermeasures, high-precision positioning in GPS-denied environments, integration into smartphones, and advanced disaster monitoring. Compared with quartz oscillators, NTP, or GPS-based timekeeping, CSACs reduce errors by 4‑8 orders of magnitude. By equipping each sensor device with a CSAC and implementing timestamping mechanisms, synchronized data collection can be achieved even when GPS is inaccessible, wireless connections are unstable, and wired networks are unavailable. Previous developments incorporated an analog MEMS accelerometer and allowed connection of arbitrary analog sensors through an external interface. However, the limited accuracy of MEMS accelerometers and the noise susceptibility of analog signals led to the development of a fully digital platform. Specifically, a digital accelerometer was integrated to allow high-sensitivity measurements without noise, while a camera sensor was supported. Both digital outputs were precisely timestamped using the CSAC. The resulting synchronized data can be applied to civil infrastructure inspection and structural health monitoring.

III. DEVELOPED AUTONOMOUS TIME-SYNCHRONIZED SENSING SYSTEM AND TIME SYNCHRONIZATION MECHANISM

As shown in Figure 1, the developed sensor device consists of an oscillator and a Field-Programmable Gate Array (FPGA) that synchronize GPS time (GPST) with the CSAC, supply stable reference signals, and maintain absolute time; a sensor section with a digital accelerometer and analog input interface; a signal processing board with a CPU; and a camera. The oscillator and FPGA provide a high-precision 10 MHz reference clock and a 1 pulse-per-second (PPS) signal. The FPGA generates timestamps and trigger signals for data acquisition. The sensor section comprises a digital accelerometer and an external analog input interface, allowing the connection of arbitrary analog sensors. The digital accelerometer outputs data in response to trigger signals via UART. Signals from external analog sensors are converted by A/D converters and output as 16-bit serial values. The camera sensor captures images in response to trigger signals and outputs RGB data. Data are stored on solid-state drives (SSDs), with separate SSDs for sensor and camera data to optimize access speed. Data can be retrieved, deleted, or viewed via network connections. Network options include wired LAN and Wi-Fi.

The mechanism of time synchronization in this system is described below. As shown in Fig. 2, the devices are divided into a master and slaves. First, the CSAC (Chip-Scale Atomic Clock) of the master device is synchronized to GPS. The master device connects to a GPS antenna and feeds the 1 PPS signal output from the GPS module into the CSAC. Through the built-in synchronization function of the CSAC, both the 1 PPS and 10 MHz signals generated by the CSAC are aligned with the GPS. Depending on GPS reception conditions, the time offset between the GPS and CSAC 1 PPS signals remains within 50 ns. If synchronization is performed too frequently, short-term fluctuations of the GPS signal dominate and the holdover performance deteriorates. Therefore, in this system, synchronization is carried out at intervals of 1000 seconds. The slave devices receive the 1 PPS signal from the master's CSAC and synchronize in the same manner. Since the 1 PPS signal generated by the master's CSAC is more stable than the GPS itself, the time offset with respect to the master device remains within 10 ns. Through this process, the CSAC effectively functions as a GPS-equivalent time source, and the CSACs of both the master and slave devices achieve high-precision synchronization.

By operating with a clock synchronized at high accuracy using the CSAC, sensor devices can maintain absolute time information (timestamps). As shown in Fig. 3, the master device first acquires absolute time information from the GPS module in the format defined by the National Marine Electronics Association (NMEA), which is a standard for data exchange between GPS and marine-related equipment. The master then transfers this time information to the Real-Time Clock (RTC) implemented in the FPGA and starts the seconds count using the 1 PPS signal from the CSAC, already synchronized to GPS. As a result, the count starts at the timing of the 1 PPS signal, the timestamp is aligned with the 1 PPS,

and the clock advances based on the 10 MHz signal from the CSAC. The slave devices obtain the time information from the master via NTP or manual configuration, set it in their CPU clock, and forward it to the FPGA. From this point onward, they operate in the same manner as the master device.
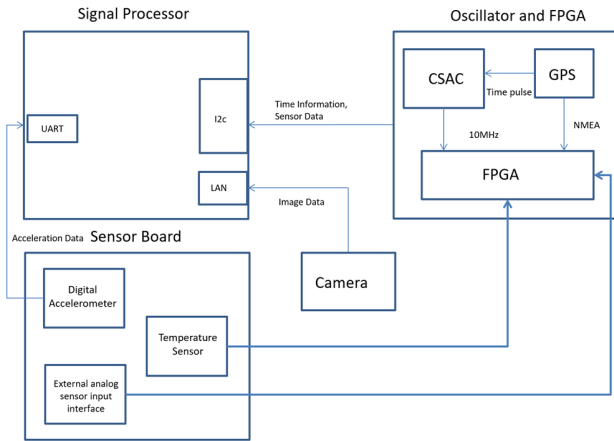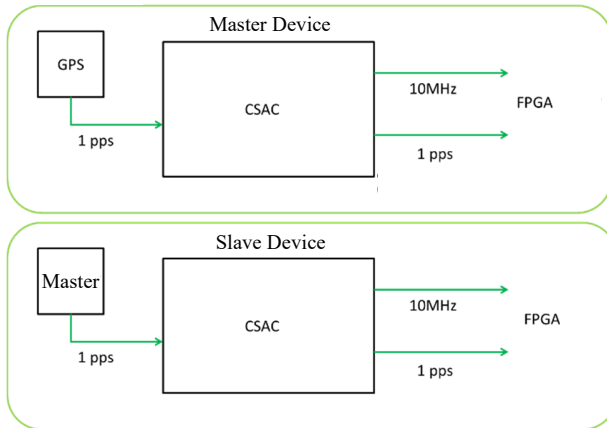

Figure 1.   System configuration.
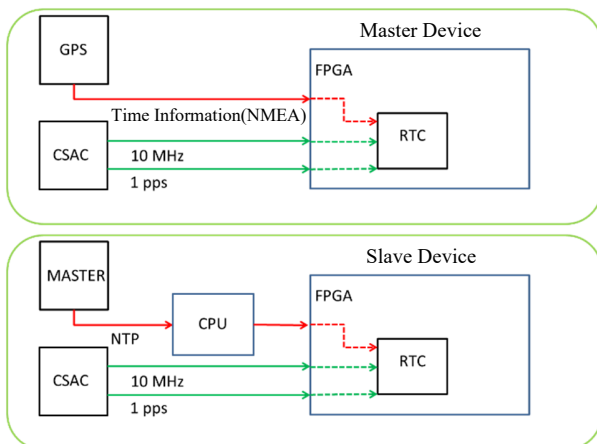

Figure 2.   Synchronization of clock.

Figure 3.   Synchronization of time information(time stamp).

Table I summarizes the specifications of the camera sensor, the Baumer VCXG-02C, a compact, low-power, high-speed Gigabit Ethernet camera [6]. It features excellent performance in low-light conditions, supports external trigger input, and includes a retransmission buffer for stable data transfer. Its global shutter mechanism enables accurate timestamping of images by capturing entire frames simultaneously, avoiding temporal distortions associated with rolling shutters.

TABLE I.   SPECIFICATIONS OF CAMERA SENSOR

Model	Baumer VCXG-02C
Active Array Size	640 x 480
Sensor	CMOS ON Semiconductor： PYTHON 300
Pixel Size	4.8 μ m x 4.8 μ m
Shutter	Global Shutter
Power Supply	12-24 VDC/2.6W
Image Formats	BayerRG / RGB / BGR / Mono
Frame Rate(fps)	401(640 x 480)
Exposure Control	20μsec ～ 1sec
Operation Mode	Trigger/Free Run
Size(mm)	29 × 29 × 49
Weight(g)	120
Interface	GigabitEthernet（1000BASE）/ FastEthernet（100BASE）

IV.   TIME SYNCHRONIZATION PERFORMANCE TEST BETWEEN CAMERA SENSOR AND EXTERNAL ANALOG INPUT SENSOR

In this section, the synchronization performance between the camera sensor and external analog input sensors is evaluated in detail. The purpose of the experiments is to verify whether both sensing modalities, despite differing in sampling characteristics and data acquisition timing, can be assigned unified timestamps that accurately represent the same physical phenomenon. As shown in Figure 4, three developed sensor boards were mounted on a vibration testing apparatus, together with a specially designed LED visualization board. The vibration table was driven by a sine wave excitation signal, which was simultaneously fed into the external analog input interface of the sensor boards and the FPGA controlling the LED board. The FPGA controlled the LED lighting pattern in real time, based on the amplitude of the input sine wave. This setup ensured that the LED illumination served as a visual representation of the vibration waveform, allowing direct comparison with the analog sensor data and camera images. The excitation waveform was a 1 Hz sine wave. Since the timestamps of the camera images and analog sensor measurements were synchronized using the CSAC, comparing the LED images captured by the camera with the vibration waveforms measured by the analog sensor enabled direct evaluation of timestamp accuracy and potential delays.

The camera sensor was configured to operate in external trigger mode. The image acquisition process followed the sequence: trigger input (shutter) → exposure → data readout. The timestamps were appended when the CPU acquired the complete image frame. As a result, a small inherent delay occurred depending on the exposure duration. For these experiments, the camera was configured to capture frames every 20 ms, while the analog sensor was sampled every 1 ms. This setup allowed verification of synchronization within a resolution of 20 ms.

To visualize the sinusoidal input signal, the LED board, shown in Figure 6, consisted of 50 LEDs (25 green and 25 red). A single sine wave cycle was divided into 50 segments, with LEDs arranged in a circular pattern and illuminated sequentially in a counterclockwise direction. This arrangement enabled a rotating light pattern corresponding to the instantaneous phase of the sine wave. The mapping of input voltage to LED illumination was pre-calibrated using approximately 20 sampled sine waves, ensuring that LED lighting accurately represented the vibration amplitude.

Initial experiments used a synthesized 1 Hz sine wave to validate the system. Camera images of the LEDs confirmed that transitions occurred in accordance with the expected waveform progression. As shown in Figures 9 and 10, the LED positions captured by the camera corresponded to the positive and negative peaks of the sine wave. The analog sensor data recorded in parallel are shown in Figure 11. Comparison with the analog sensor waveforms indicated a delay of approximately 2 ms between the two measurement modalities, which is well within the 20 ms threshold. This confirmed that synchronized timestamping between the camera and analog sensor was functioning as intended.

Further experiments were conducted using the vibration table to replicate realistic conditions. As shown in Figure 5, the three sensor boards were rigidly mounted to the vibration platform. The excitation signal was simultaneously applied to the analog input interface of the sensor boards and to the LED control FPGA. Camera images obtained during vibration are presented in Figures 12 and 13, corresponding to the maximum and minimum points of the sinusoidal vibration cycle. The analog sensor data recorded in parallel are presented in Figure 14.

From Figures 12–14, the maximum value of the analog sensor waveform occurred at 268 ms, while the corresponding maximum indicated by the LED pattern in the camera images was observed at 260 ms. This corresponds to an offset of 8 ms. Similarly, the minimum value of the analog waveform occurred at 773 ms, while the LED-based minimum occurred at 760 ms, corresponding to an offset of 13 ms. Both offset values fall within the 20 ms resolution limit imposed by the camera's frame interval. Thus, the results confirm that synchronization accuracy between the camera images and analog sensor data was maintained.

The detailed experimental validation demonstrated that the developed autonomous sensing system, employing a CSAC for timestamp generation, successfully achieved synchronization between heterogeneous sensor modalities—specifically, the camera sensor and external analog sensors. Although small offsets of several milliseconds were observed

due to the camera's exposure and frame acquisition process, these offsets were consistently within the 20 ms limit, thereby confirming the effectiveness of the proposed system.
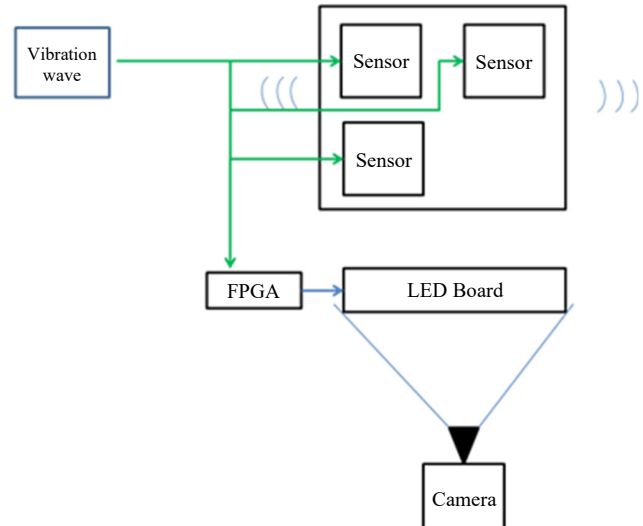

Figure 4.   Block diagram of vibration wave time synchronization verification test system.
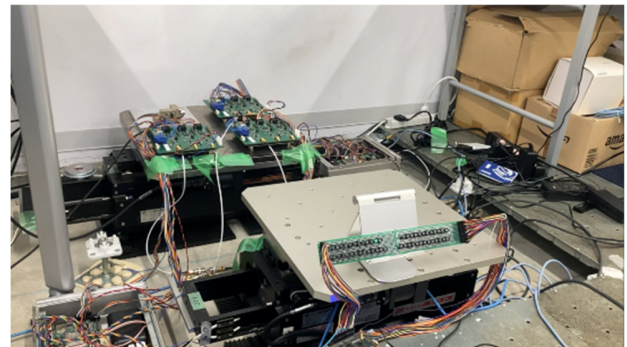

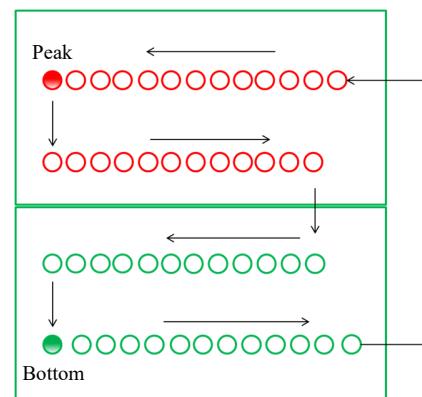Figure 5.   Vibration wave time synchronization verification test system.

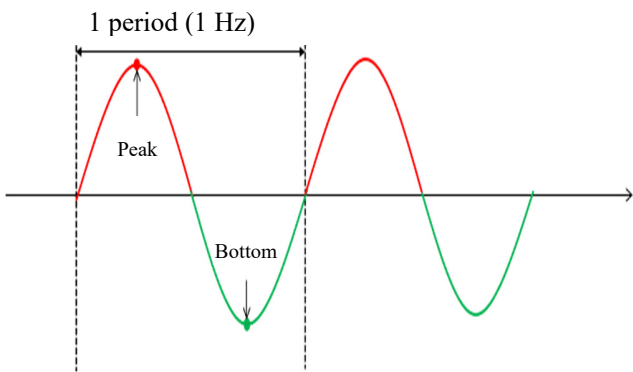Figure 6.   LED board diagram.

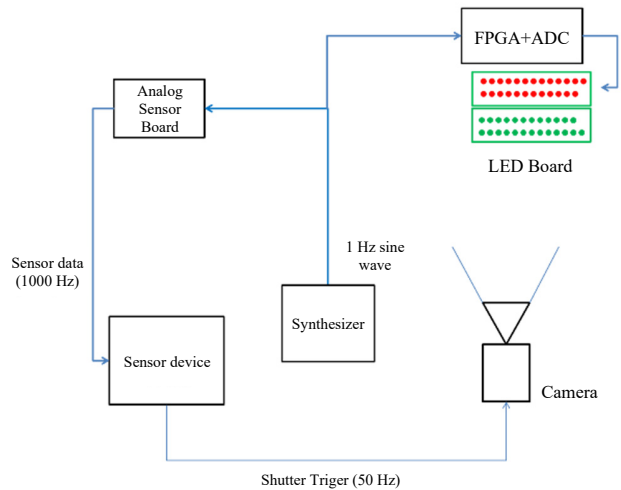Figure 7.   Waveform and LED.

Figure 8.   Synthesizer-based measurement system.
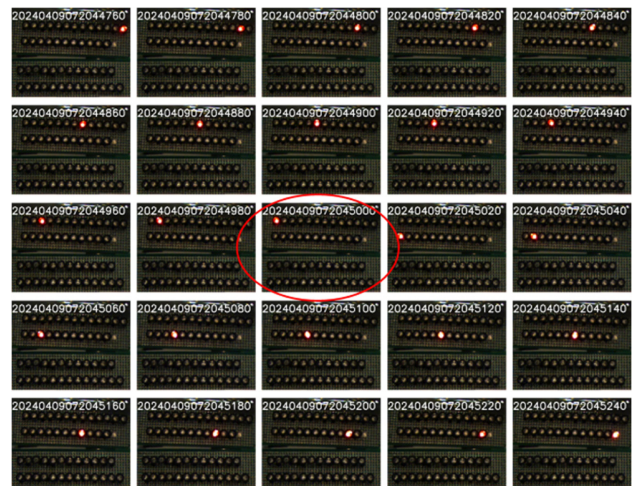

Figure 9.   Image of an LED (first half of the sine wave).
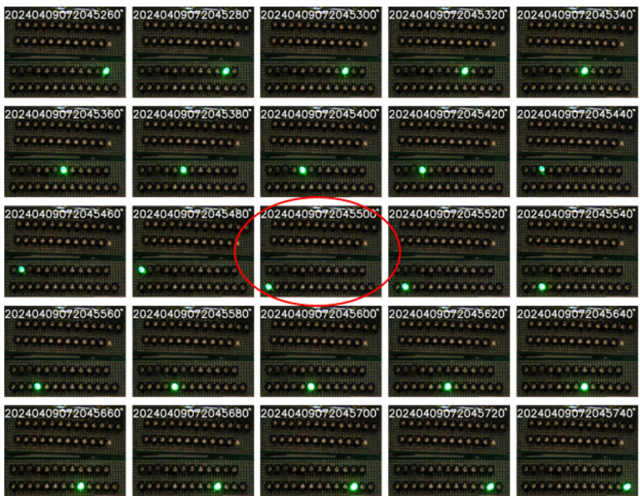

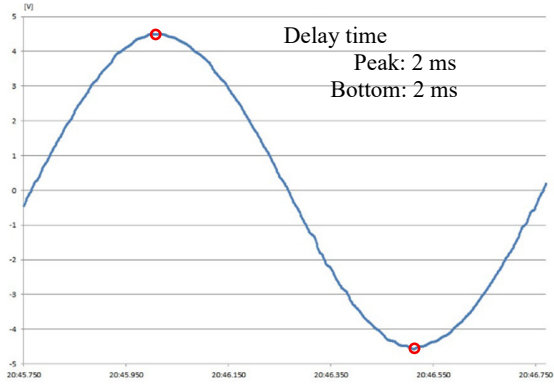Figure 10. Image of LED (second half of sine wave).

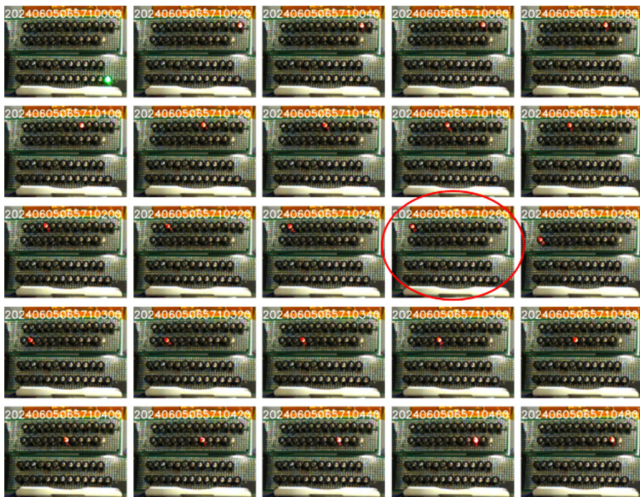Figure 11. Measurement data using external analog sensor interface

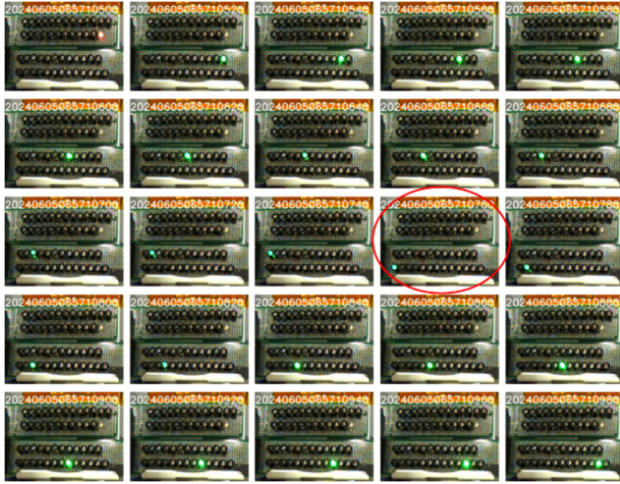Figure 12. Image of an LED (first half of the sine wave).

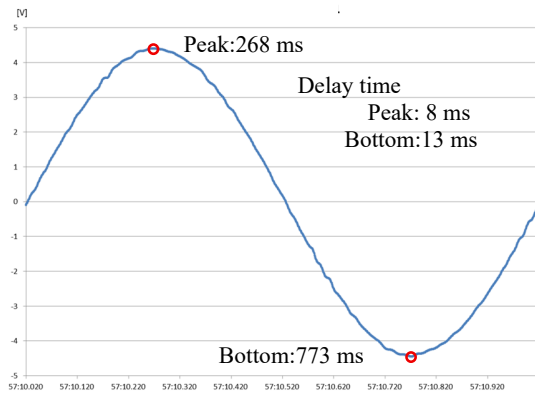Figure 13. Image of LED (second half of sine wave).

Figure 14. Measurement data using external analog sensor interface.

V. CONCLUSION

In this paper, the mechanism of time synchronization and the details of evaluation experiments for an autonomous sensing system equipped with a CSAC (Chip-Scale Atomic Clock) that provides highly accurate absolute time information were reported. First, the developed autonomous time synchronization sensor device, the synchronization method, and the approach for attaching high-precision absolute timestamps to sensor data using the CSAC were described in detail. A function was implemented to assign identical timestamps to the outputs of the camera sensor, the internal digital accelerometer, and the external analog input interface, and the experimental results for verifying the time synchronization performance of the camera sensor were reported.

Through the outcomes of this study, it was demonstrated that even in environments where GPS signals cannot be received and the installation of dedicated wiring or network infrastructure is infeasible, the sensor device can autonomously maintain absolute time information and ensure the acquisition of time-synchronized measurement data. Such sensor data can be utilized for analyses based on inter-data phase information as well as for time-series analysis. However, accurate time information cannot be permanently preserved by CSACs, as degradation due to aging occurs. Therefore, periodic re-synchronization must be performed, and efficient operational strategies must be considered. Rather than short-term ultra-high-precision synchronization, the development of a new type of CSAC offering moderate accuracy with long-term stability is considered desirable.

In future research and development, the time synchronization performance of this new sensor device will be examined in detail across three channels: the camera sensor, the internal digital accelerometer, and the external analog input sensor.

REFERENCES

[1] N. Kurata, "Development of An Autonomous Time-synchronized Sensing System Capable of Measuring Acceleration and Images" The Fourteenth International Conference on Sensor Device Technologies and Applications (SENSORDEVICES 2023) IARIA, Sep. 2023, pp.30-37, ISSN: 2308-3514, ISBN: 978-1-68558-091-9.

[2] N. Kurata, "Basic Study of Autonomous Time Synchronization Sensing Technology Using Chip Scale Atomic Clock," 16th International Conference on Computing in Civil and Building Engineering (ICCCBE2016) ISCCBE, July 2016, pp. 67-74.

[3] N. Kurata, "An Autonomous Time Synchronization Sensor Device Using a Chip Scale Atomic Clock for Earthquake Observation and Structural Health

[4] Monitoring" The Eighth International Conference on Sensor Device Technologies and Applications (SENSORDEVICES 2017) IARIA, Sep. 2017, pp.31-36, ISSN: 2308-3514, ISBN: 978-1-61208-581-4.

[5] N. Kurata, "Seismic Observation and Structural Health Monitoring of Buildings by Improved Sensor Device Capable of Autonomously Keeping Accurate Time Information," International Journal on Advances in Systems and Measurements, IARIA, vol 12, no 1&2, pp. 41-50, 2019.

[6] N. Kurata, "Digital Sensing Platform with High Accuracy Time Synchronization Function for Management of Buildings and Cities," The Tenth International Conference on Sensor Device Technologies and Applications (SENSORDEVICES 2019) IARIA, Oct. 2019, pp. 53-58, ISSN: 2308-3514, ISBN: 978-1-61208-745-0

[7] N. Kurata, "High-precision Time Synchronization Digital Sensing Platform Enabling Connection of a Camera Sensor," The Twelfth International Conference on Sensor Device Technologies and Applications (SENSORDEVICES 2021) IARIA, Nov. 2021, pp. 98-104, ISSN: 2308-3514, ISBN: 978-1-61208-918-8

[8] S. Knappe, et al., "A Microfabricated Atomic Clock," Applied Physics Letters, vol. 85, Issue 9, pp. 1460-1462, Aug. 2004, doi:10.1063/1.1787942.

[9] Q. Li and D. Rus, "Global Clock Synchronization in Sensor Networks," IEEE Transactions on Computers, vol. 55, Issue 2, pp. 214-226, Jan. 2006, ISSN: 0018-9340.

[10] R. Lutwak, et al., "The Chip-Scale Atomic Clock - Prototype Evaluation," 39th Annual Precise Time and Time Interval (PTTI) Meeting, Nov. 2007, pp. 269-290.

[11] D. Mills, "Internet Time Synchronization: the Network Time Protocol," IEEE Transactions on Communications, vol. 39, Issue 10, Oct. 1991, pp. 1482-1493, doi:10.1109/26.103043.

[12] M. Maroti, B. Kusy, G. Simon, and A. Ledeczi, "The Flooding Time Synchronization Protocol," Proc. the 2nd International Conference on Embedded Networked Sensor Systems (SenSys '04) ACM, Nov. 2004, pp. 39-49, doi:10.1145/1031495.1031501.

[13] J. Spilker Jr., P. Axelrad, B. Parkinson, and P. Enge, "Global Positioning System: Theory and Applications," Vol. I, American Institute of Aeronautics and Astronautics (AIAA), 1996, ISBN: 978-1-56347-106-3.

[14] J. Elson, L. Girod, and D. Estrin, "Fine-Grained Network Time Synchronization using Reference Broadcasts," Proc. 5th Symposium on Operating Systems Design and Implementation (OSDI'02), Dec. 2002, pp. 147-163, doi:10.1145/844128.844143.

[15] S. Ganeriwal, R. Kumar, and M. B. Srivastava, "Timing-sync Protocol for Sensor Networks," Proc. the 1st International Conference on Embedded Networked Sensor Systems (SenSys '03) ACM, Nov. 2003, pp. 138-149, doi:10.1145/958491.958508.

[16] K. Romer, "Time Synchronization in Ad Hoc Networks," Proc. the 2nd ACM International Symp. on Mobile Ad Hoc Networking & Computing (MobiHoc'01) ACM, Oct. 2001, pp. 173-182, doi:10.1145/501436.501440